Distribution Category:
Magnetic Fusion Energy—Environment
and Safety Analysis (UC-20e)

ANL/FPP/TM-111

ARGONNE NATIONAL LABORATORY
9700 South Cass Avenue
Argonne, Illinois 60439

FUSION REACTOR SAFETY STUDIES—FY 1977

Compiled and Edited by J. B. Darby, Jr.

Major Contributions by
J. N. Brooks, I. Charak, R. G. Clemmer,
D. Ehst, S. D. Harkness, R. H. Land,
V. A. Maroni, J. H. Norem, D. L. Smith,
H. C. Stevens, and L. R. Turner

Fusion Power Program
Argonne National Laboratory

and

J. M. Mintz
Fusion Division
General Atomic Company
San Diego, California 92138

April 1978

Table of Contents

Table of Contents (Continued)

List of Figures

List of Figures (Continued)

List of Tables

FUSION REACTOR SAFETY STUDIES - FY 1977

Abstract

This report reviews the technical progress in the fusion reactor safety studies performed during FY 1977 in the Fusion Power Program at the Argonne National Laboratory. The subjects reported on include safety considerations of the vacuum vessel and first-wall design for the ANL/EPR, the thermal responses of a tokamak reactor first wall, the vacuum wall electrical resistive requirements in relationship to magnet safety, and a major effort is reported on considerations and experiments on air detritiation.

1.0 INTRODUCTION

The eventual commercialization of fusion power reactors will require in-depth safety analyses similar to today's requirements for LWR's and LMFBR's. It is important that potential safety problems of fusion power reactors be recognized early so that safety-related criteria can guide the evolution of design philosophy. Current safety research can impact the design of experimental reactors such as The Next Step (TNS) and Experimental Power Reactor (EPR).

The scope of this activity is the identification of potential safety problems in fusion power reactors, the development of a methodology for the analysis of safety problems, the development of safety-related design criteria and the identification of research and development that is required to assure the safety of fusion reactors. The immediate effort has concentrated on the ANL/EPR to provide a focus and a degree of specificity to the studies. Safety problems associated with all major subsystems will be addressed, with initial emphasis on safety considerations of the vessel and first-wall design, the thermal responses of the reactor first wall, the magnet systems and tritium systems.

The technical progress in FY 1977 included safety considerations of the vacuum vessel and first-wall design for the ANL/EPR, the thermal responses of tokamak reactor first wall, the vacuum wall electrical resistive requirements in relationship to magnet safety and a major effort on considerations and experiments on air detritiation.

2.0 VACUUM VESSEL AND FIRST WALL DESIGN IMPACT ON SAFETY CONSIDERATIONS

2.1 Thermal Responses of Tokamak Reactor First Wall

2.1.1 First-Wall Thermal Model

The thermal transients in the ANL/EPR-76 first-wall system were studied with a modified CINDA-3G code.[1] The modeling and calculational effort was focused on two major aspects of the system: (a) quasi-steady-state temperature distribution under postulated burn-cycle conditions, and (b) transient temperature distribution under abnormal operating conditions, e.g. plasma dump on the first wall. Under part (a), two wall configurations were studied: a bare, water-cooled steel wall and a 1-cm thick graphite first wall (or liner) that radiates its absorbed energy to a water-cooled steel vacuum vessel. The peak steel and peak graphite and steel temperatures for the two cases were determined for a neutron wall loading of 1 MW/m^2, a 65-s burn time and a 30-s dwell time. Similar calculations have been performed for other values of wall loading and dwell time, as well as for variable material thermophysical properties.

2.1.2 Plasma Dump Thermal Model

The thermal effects of a plasma quench on the first wall were investigated. Since deposition of the stored plasma energy might occur over a very short burst time (e.g. milliseconds) and over less than the full first-wall area, the potential for material removal by ablation during such a burst exists. To study this phenomenon, a code developed as a component of a larger LMFBR accident analyses code was appropriately modified and used.[2] This code treats a section of the first wall in one dimension. The innermost (i.e. plasma-facing) region is considered an ablation region and is dimensioned sufficiently thick so that some material would remain even if all the energy were available to ablate the material. The region is then subdivided into as many small subregions as desired. The remainder of the wall is divided into two equally thick regions. While the model can account for the heat loss from the wall, the time scale for the burst is so short that, for practical purposes, a heat sink is ineffective.

Calculations of material ablation were done for both a steel and a graphite first wall. The heat of ablation (vaporization for steel and sublimation for the graphite) was taken as 1,564 and 14,250 cal/gm, respectively. The results are given in the following section, with the total stored energy commensurate with an average operating wall loading of 1 MW/m^2. The maximum theoretical material ablation loss (i.e., with instantaneous energy deposition) is essentially achieved for very small area fractions (e.g. $\sim$ 10%) or very short description times (e.g. $\sim$ 0.1 ms).

A more detailed description of the studies on the thermal responses of tokamak reactor first walls follows.

2.1.3 Thermal Responses of Tokamak Reactor First Walls During Cyclic Plasma Burns

2.1.3.1 Introduction

In addition to extensive radiation damage and bulk heating from high-energy neutrons, the first wall of a tokamak fusion reactor will be subjected to high surface heat loads that may affect its integrity. For a tokamak reactor operating without a divertor, a heat flux equivalent to $\sim$ 25% of the neutron wall loading will be deposited in the surface regions of the first wall during a D-T plasma burn. Under normal operation, approximately 60% of this surface heat flux will be produced by particle transport from the plasma with the remaining 40% coming from electromagnetic radiation, primarily bremsstrahlung. The absorption and removal of these large surface heat fluxes pose a major problem in the design of a high-integrity first wall. In the event of a plasma disruption, essentially all of the thermal energy in the plasma and a fraction (depending on the electrical conductivity of the wall) of the stored magnetic energy in the plasma will be deposited in the surface regions of the first wall. Because of the inherent difficulties in repairing or replacing the first wall, it seems imperative that the first wall be designed to withstand a moderate number of disruptive events.

In the present investigation two models have been developed and existing computer codes have been adapted and used to evaluate the thermal responses and operating limitations of proposed first-wall concepts under normal (cyclic)

and off-normal (plasma disruption) operation. The first-wall concepts considered include a forced-circulation-cooled stainless steel wall and a radiatively-cooled graphite liner. Appropriate materials property data used for the calculations have been obtained from the literature. The plasma performance and burn-cycle times considered are believed to be attainable in near-term experimental power reactors that operate without a divertor.[3,4] Thermally induced stresses in the first wall are a major concern during normal operation, whereas the extent of ablation of the first surface is the factor assessed for off-normal operation. The results obtained permit an evaluation of the relative merits of forced-circulation-cooled and radiatively-cooled first walls.

2.1.3.2 Model Development

Two models have been developed to analyze the thermal responses of proposed fusion reactor first-wall design concepts. One model considers the thermal responses of the first walls during cyclic plasma burns of $\sim$ 60 s. The second model considers the ablation of the wall material in the event of a plasma disruption. First wall concepts of the type proposed for near-term experimental power reactors that operate without a divertor have been analyzed.[3-5]

First-Wall Geometry. Figure 1 is a schematic diagram of the forced-circulation-cooled metal first wall analyzed in the present investigation. This concept is a general case of the Argonne tokamak Experimental Power Reactor (EPR) vacuum wall design.[4] It consists of a relatively thin ($\sim$ 2 cm) metal slab with internal channels through which a coolant is circulated to remove the heat deposited in and on the wall. The first wall may or may not also serve as the vacuum wall (the vacuum wall and coolant panel are of similar construction in the Argonne tokamak EPR). In either case it is assumed that the metal wall provides some structural support and serves as a containment for the coolant. The coolant channels in this design are parallel to the front surface. Based on earlier results,[4,6] the coolant channels are located near the plasma-side surface and are closely spaced to minimize thermal gradients in the wall. The modular units of the metal wall are 0.8-cm wide with the coolant channels covering slightly less than 50% of the equivalent front surface. The irregular shape of the front face of the metal wall, which

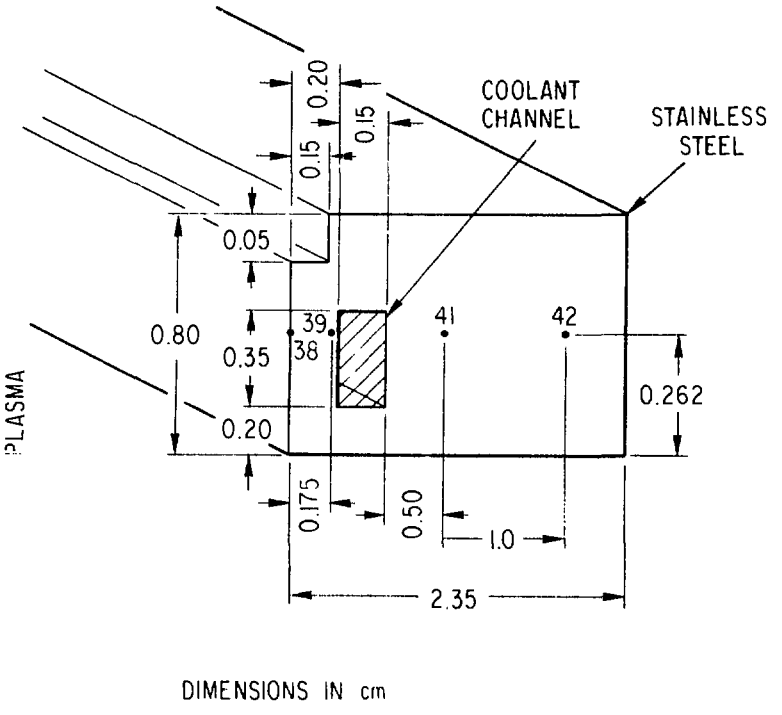

Figure 1. Schematic Diagram of Water-Cooled Stainless Steel First-Wall Design Concept.

simulates the panel coil geometry proposed for the first wall, produces only a minor variation from a smooth wall.

A schematic diagram of the radiatively-cooled graphite liner is shown in Figure 2. The liner is 1-cm thick and completely shields the structural wall from the plasma. The forced-circulation-cooled structural wall in this design is identical to the stainless steel wall described previously. Details of the liner support and the perturbations on the thermal gradients caused by the attachment of the liner to the structural wall have not been considered in the present investigation.

Model for Cyclic Plasma Burn. The CINDA-3G computer code[7] has been adapted to calculate the thermal transients in the first wall during the cyclic plasma burn. CINDA-3G is a general-purpose, three-dimensional code that solves the diffusion equation by finite-difference techniques. It is extremely flexible in that the user has available more than 100 built-in

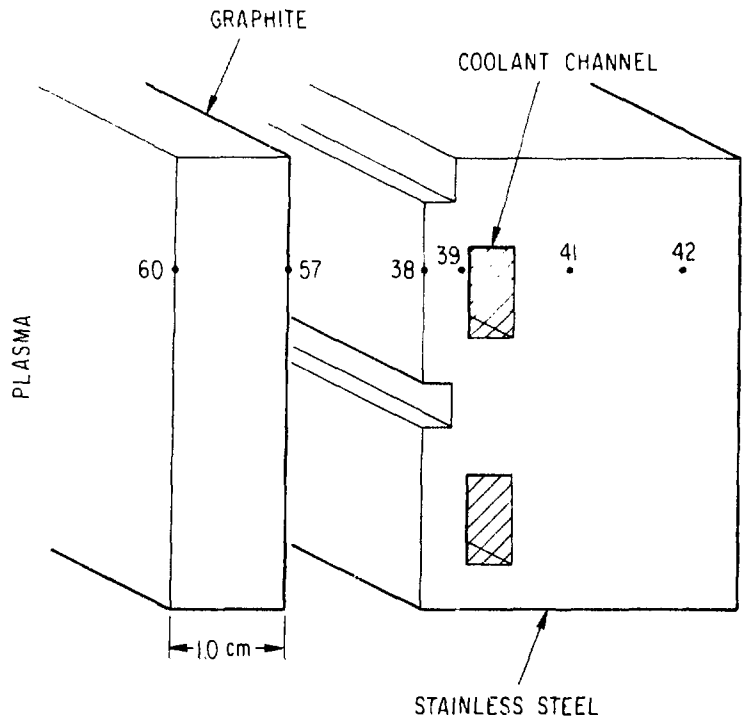

Figure 2. Schematic Diagram of First-Wall Concept With Radiatively-Cooled Graphite Liner.

subroutines to accomplish a great variety of calculations. The present model incorporates: (a) variable surface and bulk energy deposition in the wall, (b) the heat capacity of the wall material, (c) the heat conductance of the wall material, (d) thermal radiation for the case of the graphite liner, and (e) heat transport to the water coolant into the computer code to calculate the thermal response of the first wall.

Normal operation for the present analysis is a cyclic burn based on the calculated plasma performance for the Argonne tokamak EPR.[3,8] The reference burn cycle consists of a 65-s plasma burn followed by a 15-s off-time for evacuation of the plasma chamber. Figure 3 shows a simplified approximation of the power response that was derived from a complex power curve developed by Brooks.[8] The neutron power curve is represented by a ramp increase to a maximum wall loading of 1.6 MW/m^2 after 6 s, a ramp decrease to 0.75 MW/m^2 after 52 s, and a sharp ramp decrease to zero power at the end of the 65-s burn. This curve corresponds to an average neutron wall loading of 1 MW/m^2

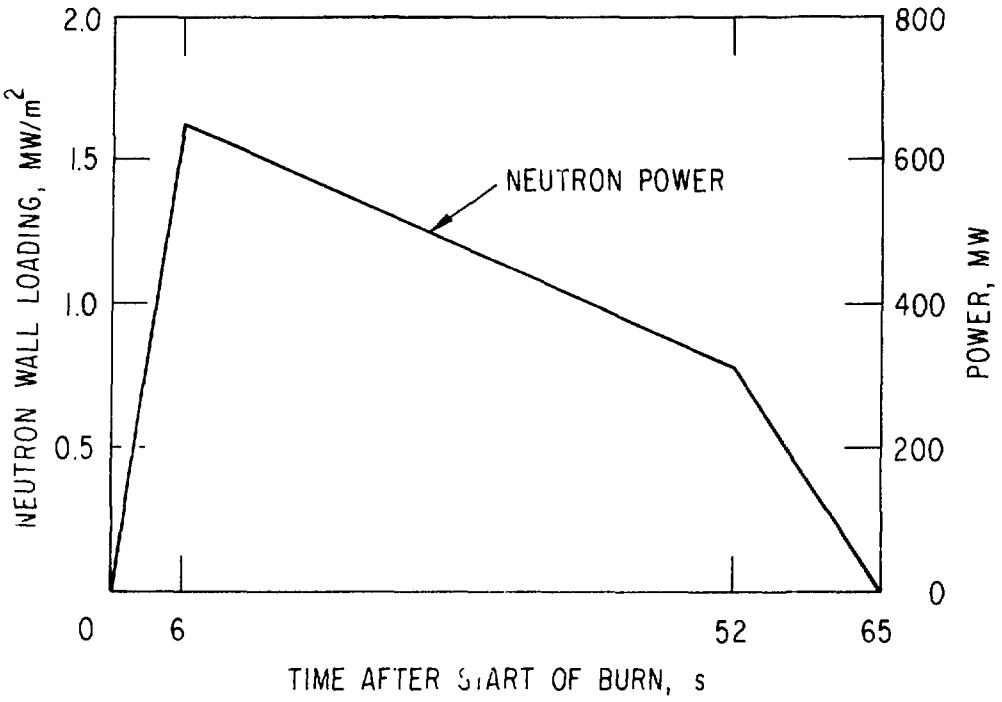

Figure 3. Power Curve for Reference Burn Cycle.

for the duration of the burn. The total neutron power of ~ 400 MW is indicated on the right-hand axis. The radiation and transport power is taken as 25% of the instantaneous neutron power.

The neutron energy is assumed to be deposited throughout the stainless steel wall giving a bulk heating rate that scales directly as the neutron wall loading. The bulk heating rate corresponding to a 1 MW/m^2 neutron wall loading is 10 W/cm^3 for stainless steel. The neutron flux, and hence the energy deposition, is attenuated exponentially through the stainless steel wall, according to the results of Abdou.[9] The neutron heating in stainless steel is reduced to about 80% at the backside of the 2-cm wall. For the case of the graphite liner, a uniform bulk heating rate of 7 W/cm^3 is used for a 1 MW/m^2 neutron wall loading.[9] No attenuation of the neutron flux is assumed for the thin graphite liner.

In the present analysis it is assumed that all of the radiation and transport power is deposited on the surface of the first wall. This is

considered to be a good approximation for the high-Z (atomic number) steel wall; however, the bremsstrahlung radiation from a high-temperature plasma will have significant penetration (hundreds of micrometers) in low-Z materials such as graphite. Although this is not expected to be a major effect in the relatively thick monolithic graphite liner, it may have important implications for thin low-Z coatings such as beryllium.[4,6]

For the case of the forced-circulation-cooled metal wall the heat is simply transferred to the water coolant and transported out of the wall. For the case of the graphite liner, the energy deposited in the liner is thermally radiated to the metal structural wall and the heat again removed by the water coolant.

Model for Plasma Disruption. An existing computer code, which was developed as a component of a larger Liquid Metal Fast Breeder Reactor (LMFBR) accident analysis code,[10] was appropriately modified and used to determine the extent of ablation of the first wall that will occur after a plasma disruption. This one-dimensional code treats the innermost, i.e., plasma side, region of the first wall as an ablative region. The thickness of this region is chosen such that some material remains under all conditions considered. The ablative region is subdivided into a desired number of subregions whereas the remainder of the wall is subdivided into two larger, equally-sized regions. Although one can account for heat loss from the wall, the time scale for the plasma dump is so short that, for practical purposes, a heat sink is ineffective. The majority of the energy deposited is accounted for by the heat capacity and the heat of vaporization (or sublimation) of the ablated subregions. Calculations have been made for both a stainless steel and a graphite first wall. Because the ablated regions are very thin (typically tens of micrometers) and the response time is very short (milliseconds), transport of any metal in the liquid form is not considered for the steel. The thin films are assumed to vaporize or resolidify in very short times. Sublimation of the graphite wall is assumed.

2.1.3.3 Materials Property Data

The materials property data required for the calculation are summarized in Table I for stainless steel and graphite. Average handbook values are used for the densities. The thermal conductivity for stainless steel was

Table I. Materials Properties for Stainless Steel and Graphite

Property	Stainless Steel	Graphite
Density, g/cm^3	7.9	2.0
Thermal Conductivity, w/m•K	20[a]	4,10,40
Specific Heat, cal/g•°K	0.12[a]	0.45
Heat of Vaporization, Kcal/mole	85	171[b]
Vaporization Temperature, °K	1700	2500
Emissivity	--	0.8
Neutron Heating, w/cm^3	10[c]	7[c]

[a] Average value. See Ref. 11 for temperature dependent value used.

[b] Heat of sublimation for graphite.

[c] Surface heating rate for 1 MW/m^2 neutron wall loading.

taken from the temperature dependent equation for unirradiated material.[11] The thermal conductivity for graphite is sensitive to the type of graphite and to neutron radiation.[12-14] Data for irradiated graphite at elevated temperatures (> 1000°C) range from 4 to 40 W/m•°K. A mean value of 10 W/m•°K has been used for the reference case. This value, which is representative of high grade graphite with 5-10% porosity, is used to account for effects expected from high helium generation. The specific heats given in the table are handbook values for the appropriate temperatures, viz., ∿ 500°C for stainless steel and ∿ 1000°C for graphite. The heats of vaporization (sublimation) are taken from thermodynamic tables and the emissivity of 0.8 is typical of many materials. Bulk neutron heating rates have been obtained from work of Abdou.[9,15]

2.1.3.4 Thermal Response of First Wall

The thermal responses of the stainless steel wall and the graphite liner are determined for several burn-cycle scenarios and the extent of surface ablation that results from a plasma disruption is determined for stainless steel and graphite first wall surfaces.

Response During Cyclic Plasma Burn. Energy deposition rates derived from Figure 3 and the materials property data from Table I were incorporated into the CINDA-3G computer code to determine the thermal responses of the first walls for cyclic plasma burns. In the present investigation a plane that intersects the coolant channel has been analyzed. This plane is represented by the node points 38, 39, 41, 42, 57 and 60 in Figures 1 and 2. Node 38 is on the plasma-side surface of the steel wall with nodes 39, 41 and 42 located in the steel wall at the positions indicated. Node 60 is on the plasma-side surface of the graphite liner and node 57 is on the back-side surface.

Figures 4-6 are plots of the thermal history for the four nodes in the steel wall during one burn cycle. Figure 4 represents the reference case with a 1 MW/m^2 neutron wall loading and an 80-s cycle time. Figure 5 shows the effect of increasing the off-cycle time from 15 s for the reference case to 30 s. Figure 6 is for the reference burn cycle but with a 2 MW/m^2 neutron wall loading. In all cases the coolant water temperature is $\sim$ 317°C. Table II summarizes some of the critical temperatures and ΔT's in the stainless steel wall. Although a stress analysis has not yet been conducted, a qualitative assessment of the thermal stress problem for the various burn-cycle scenarios can be obtained by comparing the variations in the temperature differences between nodes 38 and 39 and those between nodes 42 and 41. The longer off-cycle has very little effect on these temperature variations whereas the higher wall loading (2 MW/m^2) substantially increases the variations in the thermal gradients.

Figures 7-9 are plots of the thermal history for nodes 57 and 60 in the graphite liner during one burn cycle. The thermal response of the liner for the reference burn cycle (1 MW/m^2, 80-s cycle) and mean thermal conductivity for graphite (10 W/m•K) is shown in Figure 7. The effect of extending the off-time to 30 s (95-s cycle) is also shown in Figure 7. Figure 8 shows the effect of variations in the thermal conductivity of graphite, and Figure 9 shows the effect of increasing the wall loading to 2 MW/m^2. Critical temperatures and temperature differences obtained from this set of curves are summarized in Table III. The longer off-time slightly reduces the plasma-side surface temperature of liner and the ΔT through the liner. The thermal response of the liner is strongly dependent on the thermal conductivity of the

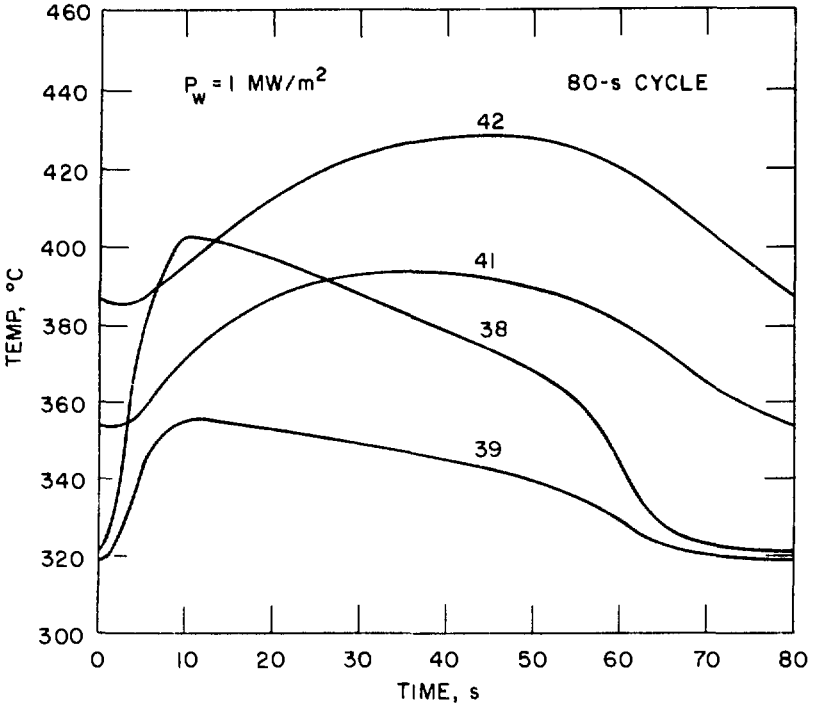

Figure 4. Temperature Response as a Function of Time for Stainless Steel First Wall During Reference Burn Cycle.

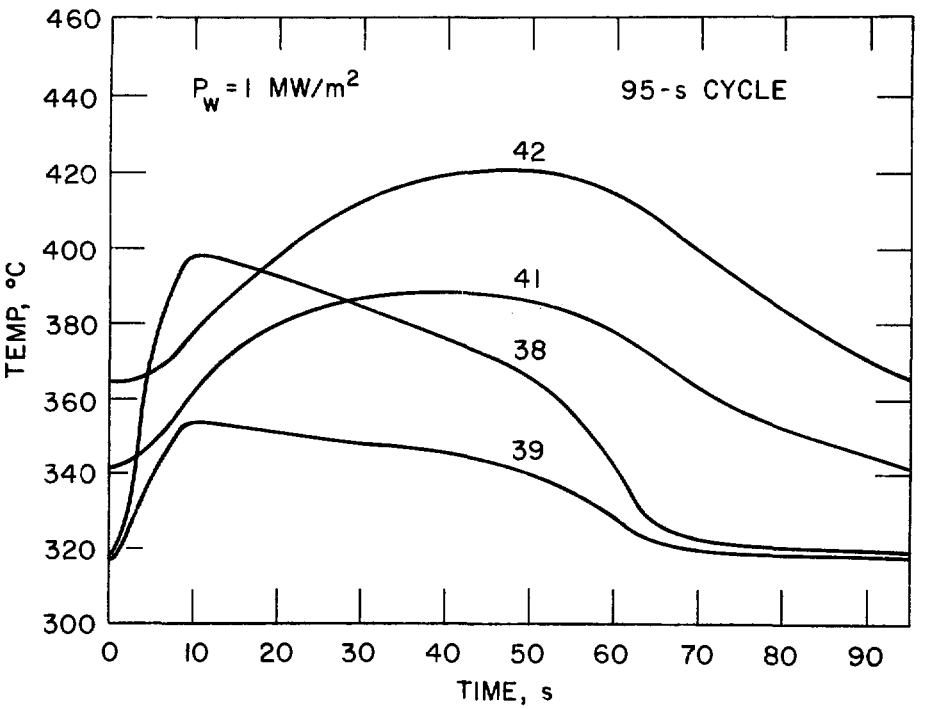

Figure 5. Temperature Response as a Function of Time for Stainless Steel First Wall During Burn Cycle with 30-s Dwell Time.

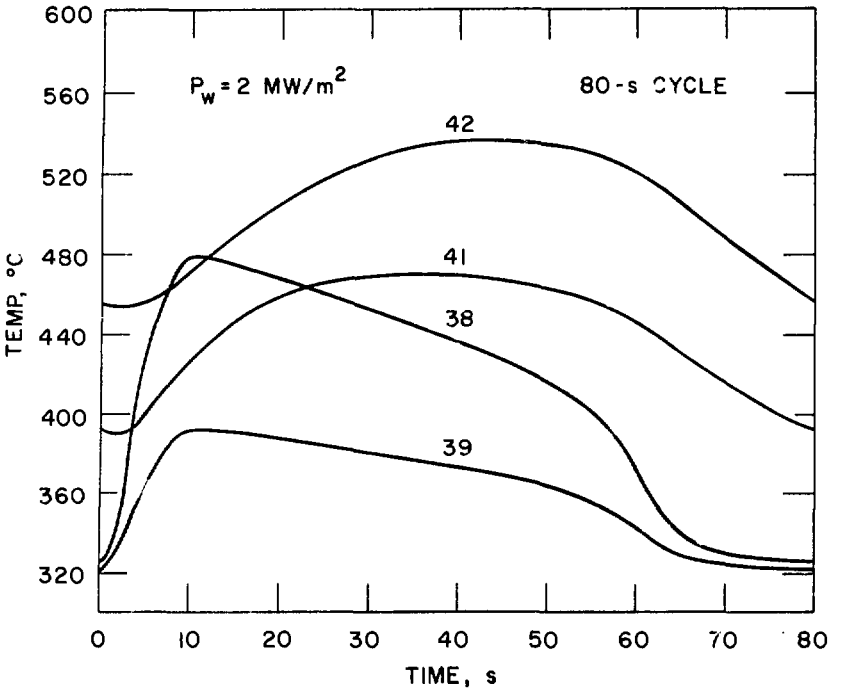

Figure 6. Temperature Response as a Function of Time for Stainless Steel First Wall with 2 MW/m^2 Average Neutron Wall Loading.

Table II. Thermal Responses of Stainless Steel Wall with No Li··r

Wall Loading, MW/m^2 Cycle Time, s	1 80	1 95	2 80
T_{max} (38), °C*	402	398	479
T_{min} (38), °C	321	319	322
ΔT_{max} (38-39), °C	48	45	87
ΔT_{min} (38-39), °C	2	1	4
T_{max} (42), °C	428	421	537
T_{min} (42), °C	386	365	454
ΔT_{max} (42-41), °C	39	37	74
ΔT_{min} (42-41), °C	23	16	43

* Numbers in parenthesis refer to nodes.

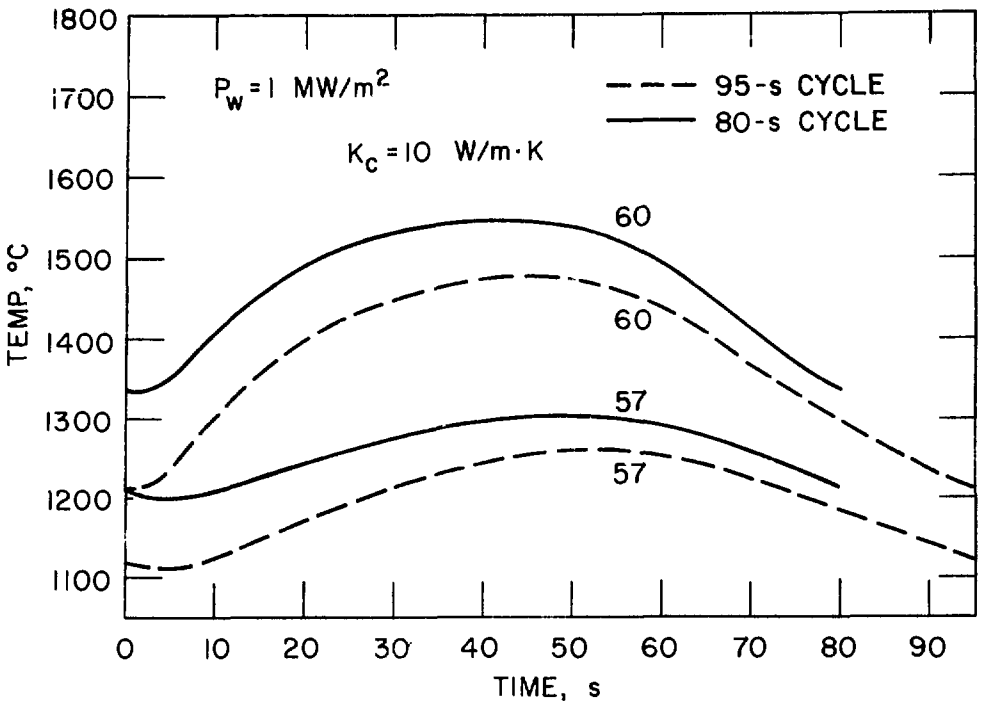

Figure 7. Temperature Response as a Function of Time for for Graphite Liner During Two Burn Cycles.

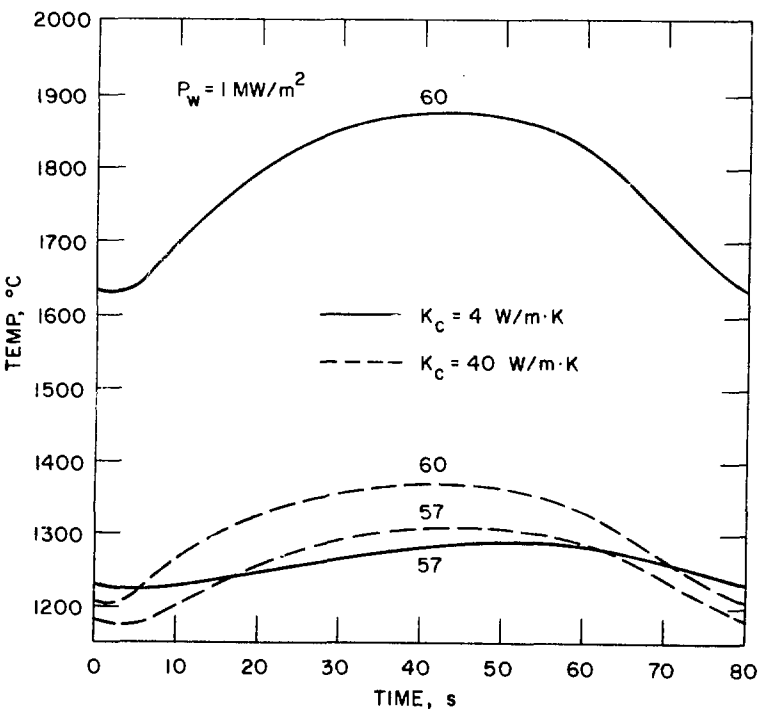

Figure 8. Temperature Response of Graphite Liner Showing Effect of Thermal Conductivity of Graphite.

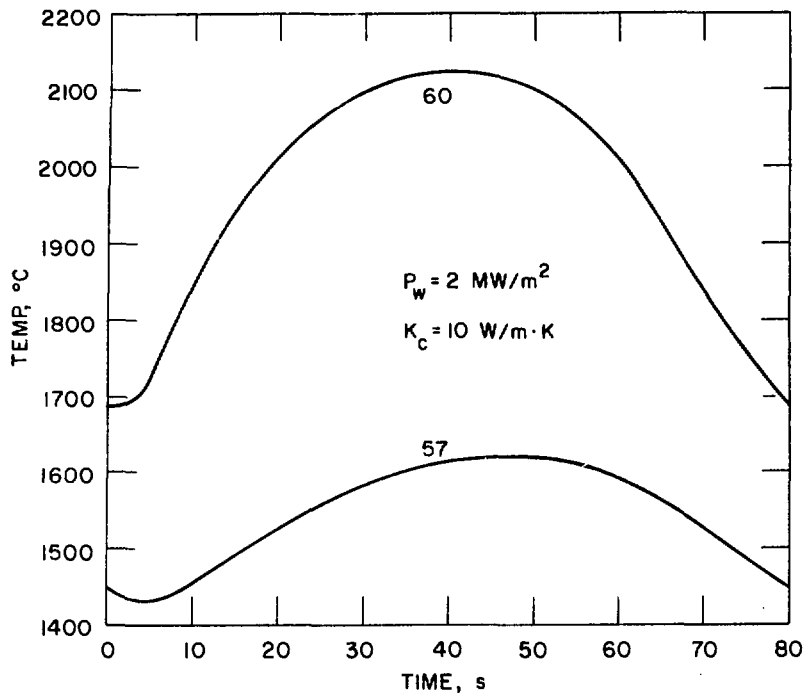

Figure 9. Temperature Response of Graphite Liner for 2 MW/m^2 Neutron Wall Loading.

Table III. Thermal Responses of Graphite for Different Burn-Cycle Scenarios

Wall Loading, MW/m^2	1	1	1	1	2
Cycle Time, s	80	95	80	80	80
K (graphite), W/m•°K	10	10	4	40	10
T_{max} (60), °C*	1545	1478	1877	1371	2123
T_{min} (60), °C	1334	1211	1631	1202	1688
ΔT_{max} (60-57), °C	256	236	594	69	516
ΔT_{min} (60-57), °C	122	92	406	24	239

* Numbers in parenthesis refer to nodes.

graphite for the range of values considered. For the low conductivity (4 W/m•K), the maximum surface temperature approaches 1880°C, which is probably unacceptable because of excessive thermal vaporization, and the maximum ΔT through the wall is nearly 600°C. This low value of thermal conductivity may be reached for highly irradiated graphite with its inherently high helium generation rates. The results are substantially different when the high thermal conductivity is used. Calculations for the 2 MW/m^2 neutron wall loading also give high values for the maximum surface temperature (2123°C) and the ΔT through the wall (516°C). This result indicates that the maximum acceptable neutron wall loading for a radiatively cooled graphite liner is substantially less than 2 MW/m^2.

Figure 10 shows a comparison of the thermal responses for the surface regions of the forced-circulation-cooled stainless steel wall with and without the graphite liner. Both the maximum temperature of the steel surface and the maximum thermal gradient in the surface regions of the steel wall are significantly decreased by the liner. This indicates that the thermal fatigue problem associated with a stainless steel first wall[4] would be reduced if a radiatively cooled liner is used. However, the lifetime of the graphite liner relative to that of the steel wall has not been evaluated for the conditions indicated.

Response after Plasma Disruption. The appropriate materials parameters have been incorporated into the plasma dump computer code to calculate the extent of ablation of the first wall in event of a plasma disruption. In the present calculation both the plasma thermal energy and the stored magnetic energy in the plasma, which are about equal, are deposited on the surface of the first wall during the dump. The time required for the plasma dump to occur and the wall area upon which the energy is deposited are not well known and probably vary with types of plasma instability. Therefore, the extent of ablation of the stainless steel and graphite walls has been calculated parametrically in terms of the dump time and the effective wall area over which the energy is deposited. Calculations have been carried out for an energy dump from a plasma that yields a 1 MW/m^2 neutron wall loading. Thicknesses of the ablated regions as functions of the two parameters are shown in Figures 11 and 12 for stainless steel and graphite, respectively.

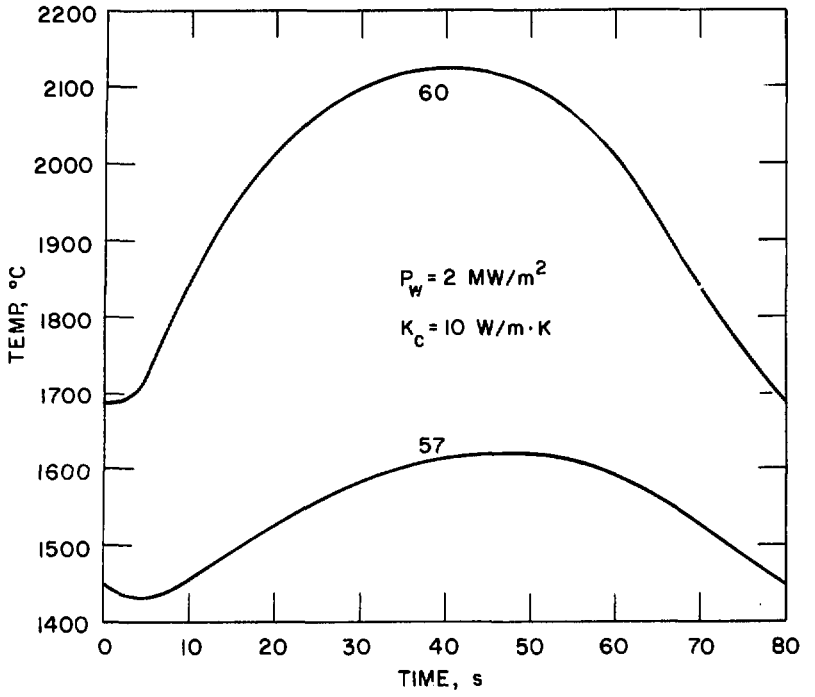

Figure 9. Temperature Response of Graphite Liner for 2 MW/m^2 Neutron Wall Loading.

Table III. Thermal Responses of Graphite for Different Burn-Cycle Scenarios

Wall Loading, MW/m^2	1	1	1	1	2
Cycle Time, s	80	95	80	80	80
K (graphite), W/m•°K	10	10	4	40	10
T_{max} (60), °C*	1545	1478	1877	1371	2123
T_{min} (60), °C	1334	1211	1631	1202	1688
ΔT_{max} (60-57), °C	256	236	594	69	516
ΔT_{min} (60-57), °C	122	92	406	24	239

* Numbers in parenthesis refer to nodes.

graphite for the range of values considered. For the low conductivity (4 W/m•K), the maximum surface temperature approaches 1880°C, which is probably unacceptable because of excessive thermal vaporization, and the maximum ΔT through the wall is nearly 600°C. This low value of thermal conductivity may be reached for highly irradiated graphite with its inherently high helium generation rates. The results are substantially different when the high thermal conductivity is used. Calculations for the 2 MW/m^2 neutron wall loading also give high values for the maximum surface temperature (2123°C) and the ΔT through the wall (516°C). This result indicates that the maximum acceptable neutron wall loading for a radiatively cooled graphite liner is substantially less than 2 MW/m^2.

Figure 10 shows a comparison of the thermal responses for the surface regions of the forced-circulation-cooled stainless steel wall with and without the graphite liner. Both the maximum temperature of the steel surface and the maximum thermal gradient in the surface regions of the steel wall are significantly decreased by the liner. This indicates that the thermal fatigue problem associated with a stainless steel first wall[4] would be reduced if a radiatively cooled liner is used. However, the lifetime of the graphite liner relative to that of the steel wall has not been evaluated for the conditions indicated.

Response after Plasma Disruption. The appropriate materials parameters have been incorporated into the plasma dump computer code to calculate the extent of ablation of the first wall in event of a plasma disruption. In the present calculation both the plasma thermal energy and the stored magnetic energy in the plasma, which are about equal, are deposited on the surface of the first wall dur ng the dump. The time required for the plasma dump to occur and the wall area upon which the energy is deposited are not well known and probably vary with types of plasma instability. Therefore, the extent of ablation of the stainless steel and graphite walls has been calculated parametrically in terms of the dump time and the effective wall area over which the energy is deposited. Calculations have been carried out for an energy dump from a plasma that yields a 1 MW/m^2 neutron wall loading. Thicknesses of the ablated regions as functions of the two parameters are shown in Figures 11 and 12 for stainless steel and graphite, respectively.

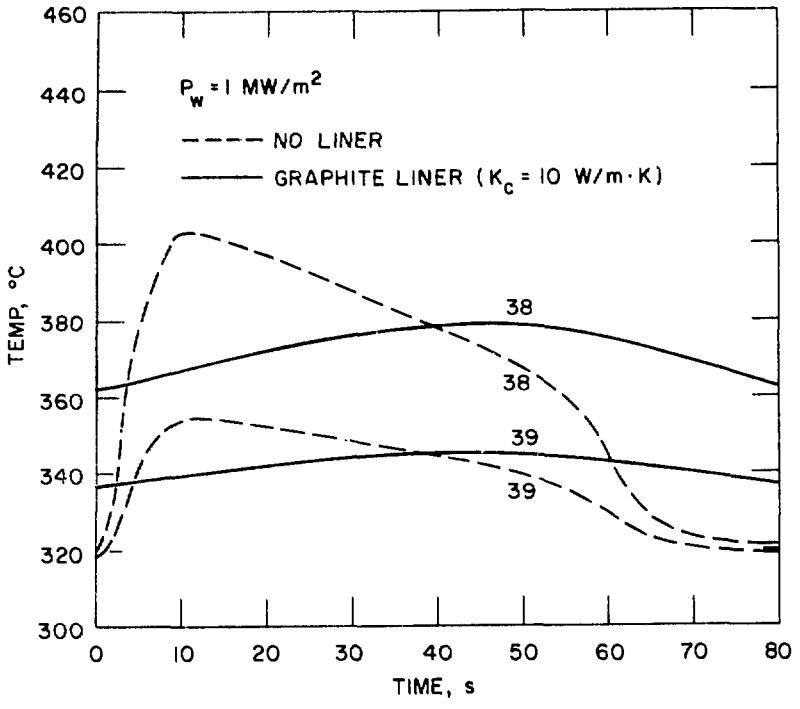

Figure 10. Temperature Response of Stainless Steel Wall With and Without Graphite Liner.

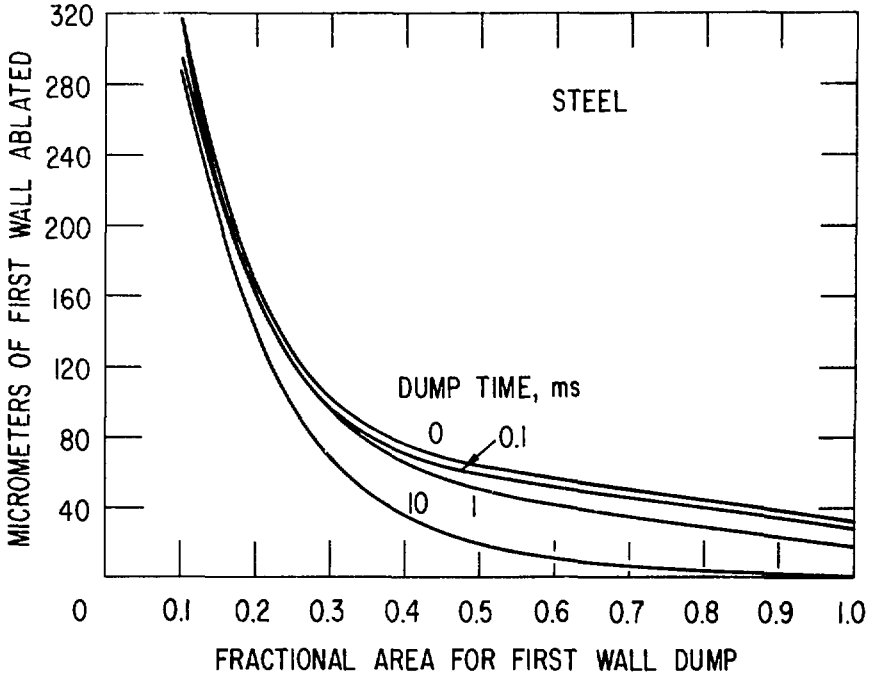

Figure 11. Thickness of Ablated Region of Stainless Steel Wall After Plasma Disruption.

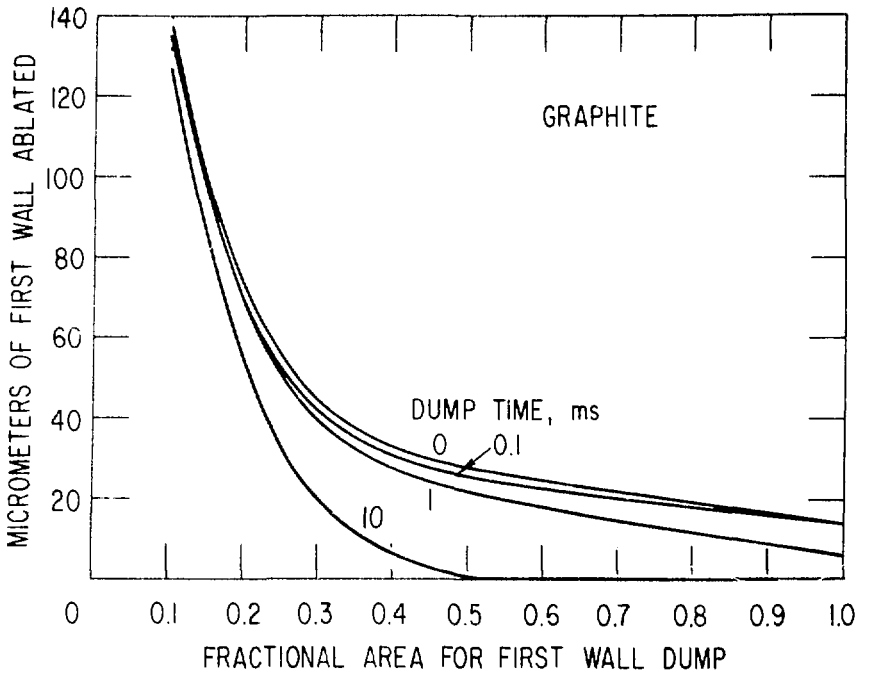

Figure 12. Thickness of Ablated Region of Graphite Wall After Plasma Disruption.

An instantaneous dump, i.e., zero dump time, does not allow for heat removal from the ablated region and, therefore, gives a maximum ablation thickness for a particular fractional wall area. For dump times up to 0.1 ms, the thickness of the ablated regions do not differ appreciably from the instantaneous dump curves. However, the 10 ms curve shows a substantial decrease in the amount of ablated material.

The fractional area of the first wall over which the plasma energy is deposited is critical. It is believed that the energy will be deposited over a major fraction (> 50%) of the wall area. For the reference case, i.e., 1.0 ms dump time, less than 50 μm of the steel wall will be ablated if the plasma energy is deposited over at least 50% of the wall. It is assumed that the deposition time is short enough and the depth of the affected region is so small that only vaporization of the steel is important. Significant transport of metal in the liquid phase is not considered for the thin regions and short dump times of interest. The ablation of graphite is generally less than half that of stainless steel for similar

conditions of dump time and effective wall area. If the plasma energy is deposited over at least 50% of the wall, the maximum ablated region is less than 30 μm for graphite.

Since all of the stored magnetic energy will probably not be deposited on the surface of the first wall, the curves in Figures 11 and 12 are conservative. Even so, results of these calculations indicate that first walls of stainless steel or graphite should withstand a moderate number of plasma disruptions if the plasma energy is effectively distributed over more than 25% of the reactor wall. This is true even if no credit is taken for redeposition of the ablated material, which is expected to occur. Also, an estimate of the capability of other first-wall materials to withstand plasma disruptions can be obtained by inserting relevant property data into the models.

2.1.3.5 Conclusions

The CINDA-3G computer code[7] has been adapted to analyze the thermal responses and oeprating limitations of two fusion reactor first-wall concepts under normal cyclic plasma burns. The first-wall design concepts considered are a forced-circulation water-cooled stainless steel panel with and without a graphite liner. For a reference burn cycle with an average neutron wall loading of 1 MW/m^2 and a coolant temperature of $\sim$ 317°C, the maximum surface temperature in the steel wall was 402°C and the maximum ΔT in the first 0.175 cm of the wall was 48°C. These values increased to 479°C and 87°C, respectively, for a 2 MW/m^2 wall loading. For the reference case the maximum surface temperature of the graphite liner was 1545°C and the maximum ΔT through the 1-cm liner was 256°C. However, these values change substantially when the thermal conductivity of graphite is varied over the range of uncertainty, viz., 4-40 W/m•°K for irradiated graphite at > 1000°C. The surface temperature of the graphite becomes unacceptably high (> 2000°K) if the lower value of thermal conductivity is used or if the neutron wall loading is increased to 2 MW/m^2 with an average value of 10 W/m•°K for the conductivity of graphite.

A component of an LMFBR computer code[10] has been modified and adapted to analyze the ablative behavior of stainless steel and graphite first walls subjected to a plasma disruption. The thicknesses of ablated regions were

determined parametrically for the two wall materials in terms of the plasma dump time and the fraction of the wall area over which the energy was deposited. If the plasma thermal energy and stored magnetic energy are deposited over more than 50% of the wall, the maximum ablated region is < 70 μm for stainless steel and < 30 μm for graphite. Since it is expected that the plasma energy will be deposited over a major fraction (> 50%) of the first wall during a disruption, it is concluded that both wall materials should withstand a moderate number of disruptive events.

2.2 Vacuum Wall Electrical Resistance Requirements - Impact on Magnet Safety Considerations

An important safety consideration is the impact of a sudden plasma quench on the equilibrium-field (EF) and ohmic-heating (OH) coils. A sudden plasma quench means a rapid change in the plasma current and, hence, a large change in the flux field coupling with the poloidal coils. This could yield a high voltage in the coils as well as a high voltage between different portions of the blanket and between the blanket and shield, which could result in electrical arcing and destructive damage. One solution would be to have a low resistance wall so that when the plasma current quenches, the induced current in the vacuum wall dies off slowly and only low voltages are generated in the system. A disadvantage of the low-resistance vacuum wall is during initiation of a plasma. If a plasma is being established and the wall resistance is low, a substantial portion of the volt-seconds intended to aid the initiation of the plasma will be deposited in the vacuum wall. In this initial study to achieve an optimum resistance in the vacuum wall, the question of having a finite wall resistance has been examined in terms of its major implications on both the normal and abnormal operation of a tokamak reactor and the details are presented in section 2.2.1.

The results of this initial study indicate that a conducting wall will be tolerable but further design studies are required to achieve an acceptable initiation-trimming coil system and a vacuum wall that can withstand the pressure and heat loads following a plasma dump.

2.2.1 Resistive Requirements for the Vacuum Wall of a Tokamak Fusion Reactor

2.2.1.1 Introduction

Most conceptual designs of tokamak power reactors have incorporated a ceramic insulator in the vacuum wall to make the wall electrically non-conducting. The purpose of this "flux breaker", as it is known, is to prevent a toroidal current from being induced in the wall by the transformer action of the various poloidal field coils. The flux breaker is typically a small ceramic strip filling a gap between the otherwise metallic structure of the wall. The flux breaker is seemingly a small part of the reactor design. If it is necessary, however, the development of a ceramic member of the vacuum boundary will require a major effort to find one that can operate successfully as part of the large toroidal wall envisioned for commercial tokamak reactors. Such a material will have to be highly resistant to radiation damage at doses up to at least 10 MW-yr/m^2 while being compatible with a coolant and a first wall whose dimensions change due to thermal cycling and radiation damage. Thus, there is considerable incentive to assess the consequences of eliminating the flux breaker from the design and having a conducting boundary instead. In this initial study the question of having a finite wall resistance has been examined in terms of its major implications on both the normal and abnormal operation of a tokamak reactor. This study has been conducted within the framework of the ANL-EPR-77 design,[16] although the results should provide some guidance for future reactors as well. The EPR design referred to is a 5-m major radius tokamak with an aspect ratio of 3.5, and with an equilibrium plasma current of 7.3 MA. The vacuum chamber is designed to accommodate a non-circular plasma with a height to width ratio of up to 1.65. The basic vacuum wall design is shown in Figure 13. It is located about 0.4 m from the plasma boundary and has an irregular polygon shape made of sixteen sections, one per TF coil interval. Variations of this design having a range of resistance values have been used in the analysis.

2.2.1.2 Effect of Conducting Wall on Normal Operation

The presence of a conducting wall will tend to interfere with the current buildup in the plasma during the startup and will tned to distort the equilibrium field supplies by the EF coil. These points have been investigated by

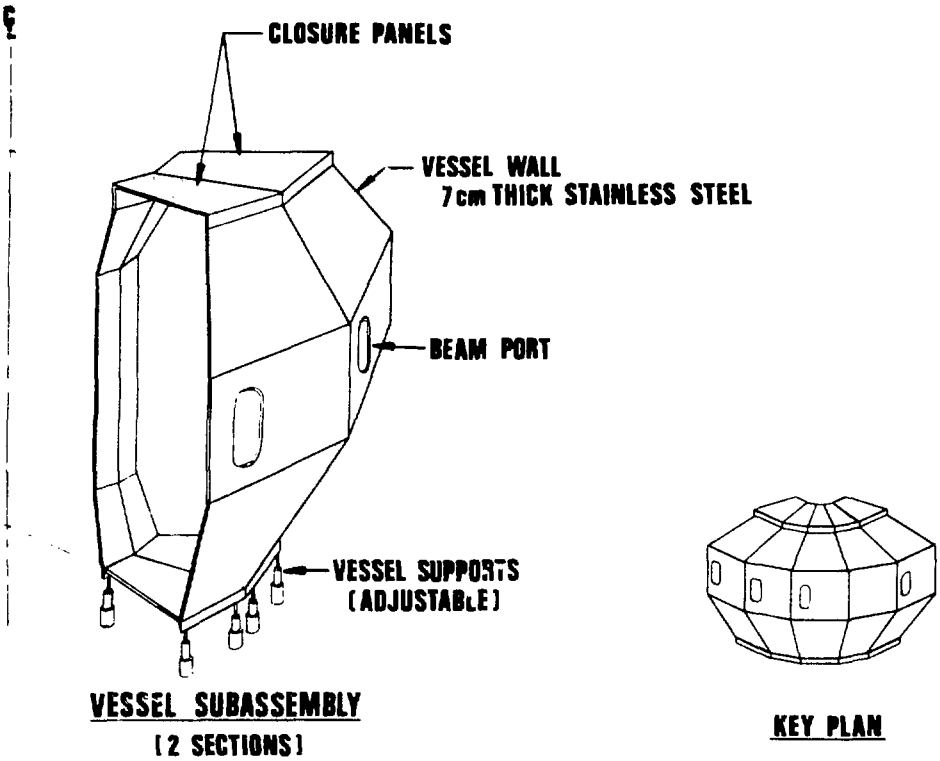

Figure 13. Basic Vacuum Wall Design

means of the equivalent circuit of the poloidal field coils, the plasma and the wall shown in Figure 14. The circuit constants pertaining to the plasma and wall are shown in Figure 14 and were computed by means of a magnetics code in which the wall was modeled by twelve inductively coupled rings and the appropriate flux linkages between coils summed to get the single-coil-equivalent parameters. Coupling terms involving the IT coil have been treated as a variable. The plasma and wall currents corresponding to Figure 13 are given by:

$$\frac{d}{dt}(L_p I_p) + R_p I_p = M_{OH,p}\frac{dI_{OH}}{dt} + M_{EF,p}\frac{dI_{EF}}{dt} + M_{IT,p}\frac{dI_{IT}}{dt} - M_{w,p}\frac{dI_w}{dt} \quad (1)$$

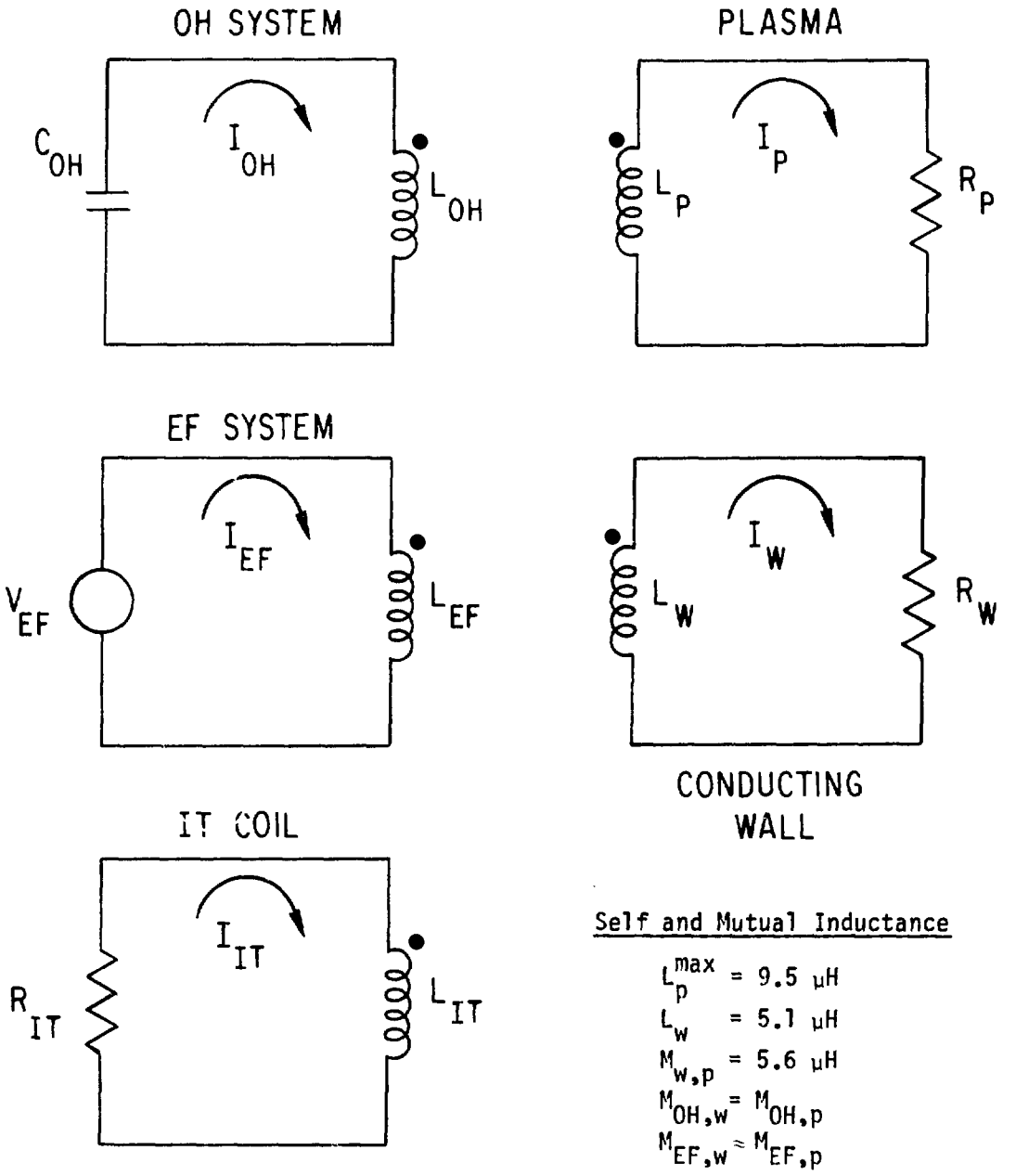

Figure 14. Equivalent Circuit of Ohmic-Heating (OH), Equilibrium-Field (EF) and Initiation-Trimming (IT) Systems; with Plasma and Vacuum Wall.

$$L_w \frac{dI_w}{dt} + R_w I_w = M_{OH,w} \frac{dI_{OH}}{dt} + M_{EF,w} \frac{dI_{EF}}{dt}$$

$$+ M_{IT,w} \frac{dI_{IT}}{dt} - M_{w,p} \frac{dI_p}{dt} \qquad (2)$$

Equations (1) and (2) and the equations for the coil currents were solved by coupling them to a plasma burn cycle code to obtain the complete behavior of the currents and the plasma during the startup. The burn cycle code solves profile average, time dependent, particle and energy balance equations for the constituent plasma particles. It includes models of radiation, transport and physics relating to the breakdown stage.

The startup of the EPR is accomplished by first establishing currents in the initiation-trimming (IT) and ohmic-heating (OH) coils by means of small power supplies (not shown). At the start of the burn cycle a resistor is connected to the IT coil and a homopolar generator (capacitor) is connected to the OH coil. The IT coil current decays rapidly, in about 8.0 ms, to provide a high voltage "blip" across the plasma. This breaks down the plasma and establishes the initial discharge current. The OH current is reversed from 0-2 seconds by means of the homopolar generator to induce a large plasma current. Beam heating is begun at 2 seconds and turned off at 6 s, at which time the plasma is at ignition. During the startup the current in the EF coil is raised to keep the plasma in MHD equilibrium as well as to induce a share of the plasma current. The effect of the conducting first wall on the initiation of the discharge and on the rest of the startup have been studied using a range of IT coil parameters and wall resistances.

2.2.1.3 Initiation Stage

For the initiation process, preliminary results indicate that for geometries similar to the ANL/EPR-77 design, an IT coil system can be built that is compatible with a conducting first wall. Different geometries of IT coils have been considered with the aim of minimizing the total stored energy and flux swing during the IT cycle. The results so far indicate that the total volt-seconds supplied by the IT coil depend critically on the ratio

$M_{IT,w}/M_{IT,p}$, the fraction of the IT flux to the plasma that also links the wall. This dependence is shown in Figure 15 for a value of $R_w \approx 700$ μΩ. This figure shows the individual and total components of the supplied volt-seconds, at the end of the 8 ms initiation period. These results were found to be fairly insensitive to the value of R_w in the range studied, that of 300-900 μΩ. Since the stored energy is proportional to the square of the supplied volt-seconds, it is important to minimize this quantity. This can most obviously be done by producing an IT coil geometry that ducts the IT flux through the first wall, however, such a system would be comparatively complex and might require coils placed between the wall and the inner leg of the TF coils. Coils in this location would complicate the construction. This problem is undergoing further study.

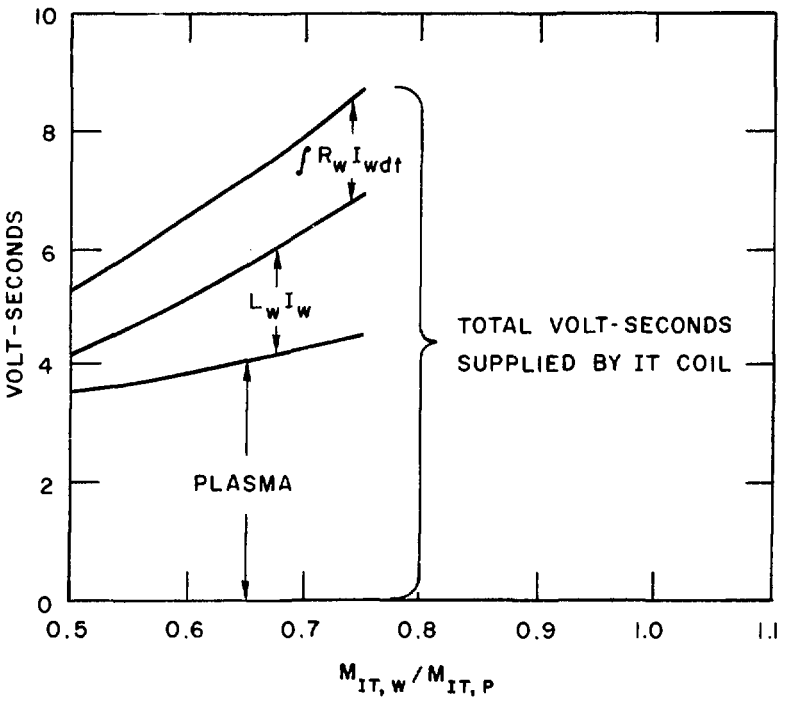

Figure 15. Initiation-Trimming Coil Requirements, with a Conducting Wall, as a Function of $M_{IT,w}/M_{IT,p}$, for an 8-ms Plasma Initiation Period.

2.2.1.4 Main Startup

For the analysis of the main startup stage a broader range of wall resistance values were examined. Figure 16 shows the effect of the wall resistance on the wall current and plasma current during the full ∿ 6-s startup. The curve of plasma current versus time corresponding to $R_w = \infty$ represents the nominal "ideal" startup using a flux breaker. It seems reasonable to require that the plasma current with a conducting wall should not deviate appreciably from the "ideal" case. The deviation is significant for R_w = 25 μΩ but is small for $R_w \geq 100$ μΩ.

Another effect of the wall current is to heat the wall, because of I^2R losses. The conducting wall also acts as a load on the OH and EF coils and so tends to increase their requirements. By the end of startup the resistively dissipated energy in the wall is 9.4 MJ for R_w = 100 μΩ and this decreases to about 1 MJ for R_w = 1000 μΩ. This range poses no significant problems. The effect on the volt-second requirements of the OH and EF coils is small for $R_w \geq 100$ μΩ.

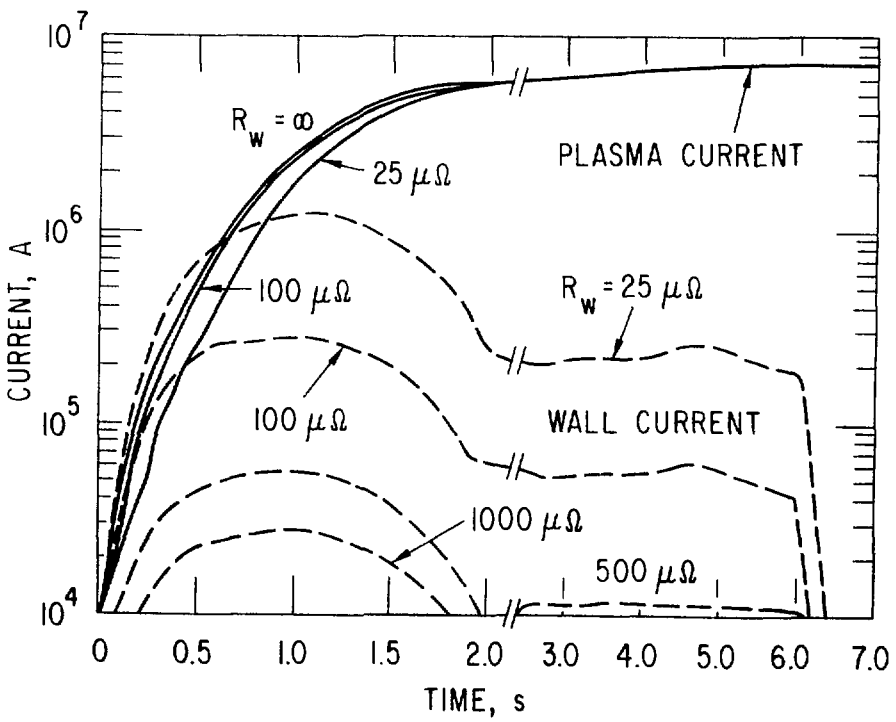

Figure 16. Plasma and Wall Currents During the Main Startup Phase for Different Values of Wall Resistance.

Another important consideration is the magnitude of the spurious magnetic fields, across the plasma region, arising from the induced wall current. This field was computed using the 12-segment wall model mentioned above. The normal peak equilibrium field, at the plasma center is 0.53 T. In comparison the maximum wall induced field is only 0.01 T for R_w = 100 μΩ. The field becomes even smaller for a higher R_w. Therefore, the induced field from the wall should not be a serious problem during the startup. (The effect on the initiation period where a null region is normally used to create the plasma may be more serious and needs additional examination.)

After the startup, during the main plasma-burn period (∿ 50 s), the OH and EF coils are quiescent and so the conducting wall does not affect this part of the burn cycle. The shutdown period is basically the reverse of the startup, in terms of the various currents so an acceptable wall resistance for startup will be acceptable for shutdown.

2.2.1.5 Abnormal Operation - Plasma Dump

A major plasma disruption or "plasma dump" is characterized by a rapid loss of plasma thermal energy and the subsequent decay of current. Eddy currents induced in a conducting wall by the decay of plasma current can be large and will cause pressure loading and heating of the wall. To evaluate these problems it is important to have a good estimate of the time scale of the dump. In the present study this estimate was made following the work of STIX[17] that leads to the prediction that the electron temperature (and current density) should vary on a time scale

$$\tau_D = \frac{C\, a^2 \pi R q}{\Delta^2} \sqrt{\frac{M_e}{2T_2}} \qquad (3)$$

Figure 17 plots experimental voltage transient times against the formula with $\Delta = 2\, q\, \rho_i$, C = 0.1 and q = 2.01, where a is the minor radius and ρ_i is the ion gyroradius, and from this scaling one expects voltage transient pulse widths of ∿ 300 μs for the EPR.

A larger number of variables seem to determine the plasma current decay time and a review of published data[18-27] reveals no obvious pattern; experimentally ΔIp occurs on a scale of tenths to tens of milliseconds. The

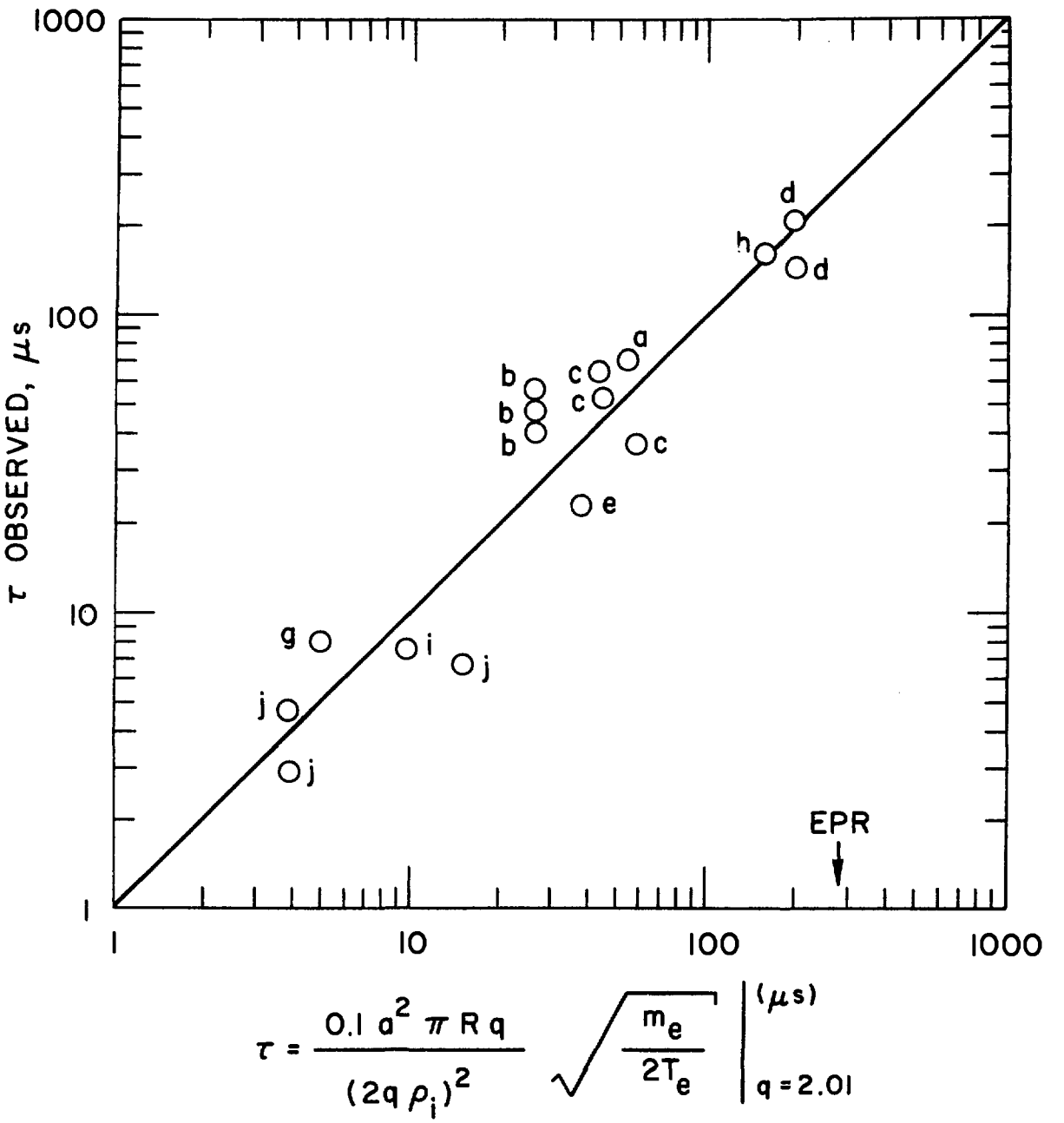

Figure 17. Voltage Transient Pulse Widths During a Major Plasma Disruption, for a Range of Tokamak Parameters. Solid Line = Formula; Circles are Experimental Data Where a-j are References 18-27, respectively.

important thing about this range of current decay times is that it is shorter than the time constant of the wall, $\tau_w = L_w/R_w$, for any feasible value of wall resistance. (For example for $R_w = 500\ \mu\Omega$, $\tau_w = 10$ ms.) A worst case analysis of the wall current induced by a plasma dump can then be made by treating the OH and EF coils as decoupled from the plasma and wall during the plasma current decay time. Under these assumptions, Equation (2) reduces to:

$$L_w \frac{dI_w}{dt} = - M_{w,p} \frac{dI_p}{dt} \tag{4}$$

Integrating Equation (4) over the decay time then gives the maximum value of wall current, for this worse case:

$$I_w^{max} = \frac{M_{w,p}}{L_w} I_p^{max} \approx I_p^{max}$$

where I_p^{max} is the value of plasma current prior to the disruption. In other words the full plasma current is transferred to the wall because of the dump.

2.2.1.6 Pressure in the Vacuum Wall After a Plasma Dump

After the dump, the wall current will interact with the magnetic field to produce a pressure in the wall. This pressure can be estimated using the following simple model.

To first order, the distribution of eddy currents induced in the vacuum wall will be such as to maintain the field unchanged outside the wall. Thus the field outside B_o will continue to be the resultant field from the previous plasma current and the EF coils, while the field B_i in the region enclosed by the wall will be the field from the EF coils alone. The pressure P acting in the wall will be

$$P = (B_i^2 - B_o^2)/2\mu_o.$$

If the wall were everywhere parallel to the magnetic field vector from the plasma current, the above argument would be correct. Because it is not,

we attempt to compensate by using only the components of B_i and B_o parallel to the wall. The resulting pressure distribution in the vacuum wall appears in Figure 18.

The pressures shown in Figure 18 are acceptable. The highest pressures are 45 psi, and thus do not appear to introduce any significant design difficulty.

2.2.1.7 Heating in the Vacuum Wall After a Plasma Dump

The current flowing in the wall, just after a plasma dump, will involve a stored magnetic energy of $1/2\ L_w I_w^2 \simeq 135$ MJ. The current will decay resistively as $I_w = I_w^{max}\ e^{-t/\tau_w}$ where τ is the time after the dump. Ohmic heating in the wall will, therefore, decay as $P_\Omega^w = I_w^2\ R_w = (I_w^{max})^2 R_w\ e^{-2t/\tau_w}$. Again, this calculation ignores the somewhat beneficial coupling to the OH and EF coils that will remove some energy magnetically from the wall. The heating is essentially over in a time $t \simeq 2\ \tau_w$ during which time the initial stored magnetic energy is converted into heat. The heating time is much shorter than the heat diffusion time of any possible wall design. Effectively, then, the wall will receive and have to survive an impulsive heat load right after the dump.

2.2.1.8 Engineering of a High-Resistance Wall

The vacuum vessel for a tokamak reactor will, in all likelihood, need to be constructed in a manner that will facilitate both assembly and disassembly. Thus, most designs are for a segmented wall of sufficient thickness to withstand anticipated normal and off-normal stresses (see Figure 13 for a typical design). In terms of controlling the resistance of the wall, the designer has three principal variables at his disposal; the choice of wall material, the wall thickness (down to some minimum determined by the material's strength), and the design of the joint between adjacent wall segments.

Three possible classes of metals for use in the construction of a vacuum wall are the austenitic stainless steels (such as annealed Type 316), the higher nickel steels (such as Inconel 625) and titanium based alloys (such as Ti-6 Al-4 V). These alloy systems offer resistivities of roughly 100, 135 and 185 $\mu\Omega$-cm at 400°C, respectively, to the designer. Allowable wall

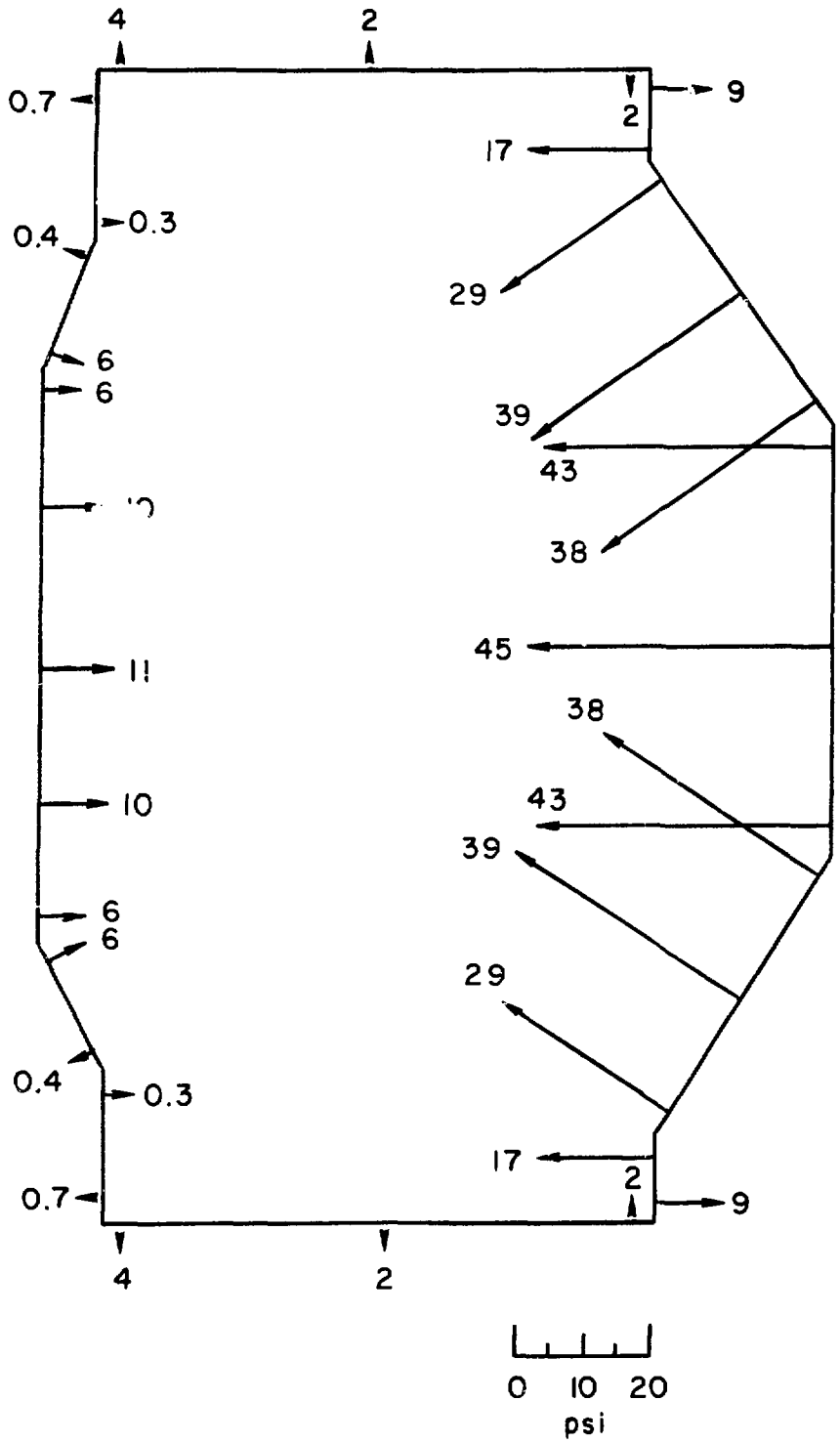

Figure 18. Pressure Distribution in Vacuum Wall Due to and Immediately Following a Major Disruption. Pressure in psi. (Center of Reactor is to the Left.)

thicknesses are a function of the strength of the material selected. Representative yield strength values for the three classes are 115, 450 and 580 MPa respectively, indicating that thinner walls may be possible if titanium alloys are used than if stainless steel is employed. Based on strength and fabrication considerations, minimum thicknesses for designs in which the vacuum wall is removed from the plasma boundary for the three possible wall materials would be about 2 centimeters for stainless steel, 1 centimeter for Inconel 625 and 0.5 centimeter for titanium alloys.

Therefore, for designs in which the joint between wall segments does not add significantly to the toroidal wall resistance, the maximum resistance attainable is about 135 μΩ for a stainless steel wall, 365 μΩ for an Inconel 625 wall and 1000 μΩ for a titanium alloy structure. Thus, continuous walls without high resistance segment joints may be possible if IN 625 or a titanium alloy is used, but are probably not feasible if stainless steel is employed. The use of a wall structure that has significant inherent electrical resistance is of great benefit in controlling the temperature rise that occurs in the wall due to the electrical currents generated by a plasma dump incident. For example, as discussed above, in the case of the ANL/EPR design, about 135 MJ are expected to be dissipated in the vacuum wall following a plasma dump. This will cause only a small temperature rise (< 10°C) in a high resistance wall such as could be constructed from titanium alloy due to the large mass of the wall. However, dissipation of this energy is an important consideration if the overall wall resistance must be achieved by the incorporation of a high resistance joint design.

For example, in the case of a stainless steel wall, to achieve an overall wall resistance of 500 μΩ, roughly 350 μΩ must be supplied by the joint between wall segments. One approach to this design problem would be to coat the portions of the wall in mechanical contact (see Figure 19) with an insulating material and provide a vacuum seal for the joint by means of a thin (and therefore resistive) piece of stainless steel that bridges the joint.

An 0.025-cm sheet of 10-cm in width between each of 16 wall segments could provide the necessary increment in wall resistance. Unfortunately, the temperature rise in these pieces due to the ohmic heating following a plasma dump would cause them to fail. A possible solution to this problem,

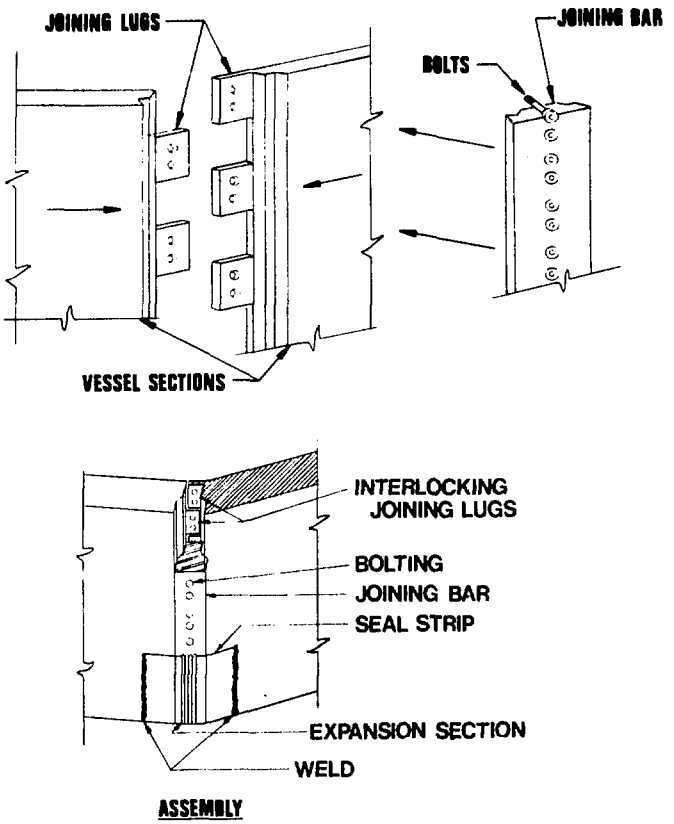

Figure 19. The Design of the Joint Between Adjacent Vacuum Vessel Segments in the ANL/EPR.

that allows the use of a stainless steel wall is the incorporation of graphite resistors into the joint design. The selection of graphite is based on its relatively high resistivity ($\sim$ 750 $\mu\Omega$-cm) and high temperature capability. A graphite layer 10-cm wide by 0.2-cm thick is envisioned to be joined mechanically to overlapping portions of the stainless steel wall at each of the 16 joints (see Figure 19). Such an addition would allow an overall wall resistance of $\sim$ 600 $\mu\Omega$ while restricting the temperature rise in the graphite due to a plasma dump to about 1000°C, which should be acceptable.

The use of such an approach probably requires the incorporation of a second vacuum boundary into the design, a precaution that is included in the ANL/EPR.

2.2.1.9 Conclusion

The effect of having a conducting vacuum wall, instead of one with a flux breaker, has been analyzed from a multidisciplinary standpoint. There is a good indication that a conducting wall will be tolerable. The most serious problems seem to be in designing an acceptable initiation-trimming coil system and in designing a vacuum wall that can withstand the pressure and heat loads following a plasma dump. There appear to be several promising design approaches for the vacuum wall that can achieve a fairly high resistance and may satisfy the latter constraints. Work is continuing on this important topic to try to further resolve these questions.

3.0 AIR DETRIATION CONSIDERATIONS AND EXPERIMENTS

A portion of the safety studies effort has been devoted to an understanding of the potential effects of various reaction and soaking mechanisms following sizable accidental tritium releases to large enclosures representative of projected fusion reactor buildings. The studies have consisted of: (1) the development of a time-dependent computer model for air detritiation analysis, (2) setting-up and performing bench-scale experiments to simulate, at least in part, the conditions anticipated for large enclosures following a tritium release, and (3) comparison of experimental and computer model results. The time-dependent computer model examines the effects of various reaction and soaking mechanisms that could occur in a typically-sized reactor building ($\sim 10^5$ m^3) following a range of tritium releases (2 to 200 gms). A parallel experimental test chamber was set up to investigate cleanup characteristics under conditions that can be simulated with the computer code. The principal value of these empirical studies is that they represent a medium with which results of actual detritiation experiments can be compared and correlated and can provide a basis for the conception, design and operation of meaningful large-scale air detritiation tests. The results indicate that while the computer analyses suggest only $\sim 10^{-3}$% of the tritium released to an ambient enclosure should be converted to tritiated water, the bench-scale experiments gave evidence of conversions to water greater than 1%. Although the amounts of soaked tritium (both calculated and observed) are usually only a very small fraction of the total tritium release, the soaked tritium is significant in that its continuous return to the enclosure extends the cleanup time beyond the predicted value in the absence of soaking mechanisms where rapid detritiation of an enclosure to the recommended radiation control guideline level (5 $\mu Ci/m^3$ for HTO) is required, there may be some incentive for venting and flushing of the enclosure towards the end of the cleanup operation.

3.1 Introduction

The need for large capacity air handling and detritiation systems to service ambient operated fusion reactor buildings is well recognized.[28-30]

The cost of such systems should scale roughly linearly with the volumetric air flow rate which is in turn determined by (1) the permissible length of time to complete a cleanup operation following the largest conceivable tritium release to a given enclosure and (2) the overall volume of that enclosure. Recent fusion reactor design and safety analyses[28-30] have uncovered at least two dominant incentives for achieving the shortest possible cleanup times. Firstly, short cleanup times would permit timely access to the reactor building when manual maintenance or repair is required, thereby reducing reactor downtime in most cases. Secondly, the amount of tritium soaked onto and into the surfaces in the reactor building is expected to increase with increasing cleanup duration and, as a consequence, the subsequent release of this "soaked" tritium could further extend the time period required to reduce the atmospheric tritium concentration to breathable levels.

An appreciable amount of experience has been gained in the design and construction of 0.5 to 5 m^3/s (10^3 to 10^4 cfm) air detritiation systems[31-34] and some analyses of catalyst performance have been done.[35-37] What has not been investigated in any detail is the actual performance of fully integrated cleanup systems during massive detritiation operations on large enclosures. In particular the impact of various chemical reaction and soaking mechanisms on the progress of the cleanup operation is not at all well understood. A series of studies to evaluate some of these factors was carried out at ANL during 1977 as part of an on-going fusion reactor safety program. The approach taken in these studies involved (1) the development of a time dependent computer model to simulate anticipated physical and chemical responses in typical enclosures following a large tritium release and (2) a series of bench scale tests with tritium in a relatively small enclosure under conditions that were intended to emulate a typical reactor building but on a much smaller scale. The following sections of this paper describe in order (1) the computational model for cleanup analyses, (2) the results of computer studies of cleanup operations on conceptual fusion reactor buildings, (3) the methodology for and results of bench scale tests with the small enclosure, and (4) attempts to analyze the bench scale data using the computer model.

3.2 Description of the Computer Model

This section contains a description of the features built into the model that was developed to simulate hypothetical air-detritiation scenarios under conditions anticipated in near-term fusion reactor containment buildings. The logic of the resulting code (TSOAK) is based largely on (1) correlations of existing experimental data for pertinent chemical and physical processes involving tritiated species with the type of phenomena likely to occur in a large enclosure, (2) derivation of a set of time dependent simultaneous equations to describe the cleanup operation, and (3) selection of an efficient algorithm to solve the resulting set of equations. The steps built into the code are summarized below:

Cleanup Operation: The principal pathway for removal of tritium-bearing species from a reactor building atmosphere following an accidental release should be the cleanup operation itself. Here it is assumed that the air in a room of volume V is circulated through a detritiation system at a volumetric flow rate Q and that the efficiency of the detritiation system for removal of tritium-containing compounds in the air (regardless of their chemical form) is ε. The rate of reduction in the concentration of any species, N_i, with time, t, by this mechanism is, therefore, given by

$$-\left(\frac{\partial N_i}{\partial t}\right)_A = \left(\frac{\varepsilon Q}{V}\right) N_i = A\, N_i \tag{5}$$

$$\text{i.e., } A = \frac{\varepsilon Q}{V} \tag{6}$$

Reaction of T_2 with H_2O and O_2: There is ample evidence to support the assumption that T_2 released to an atmosphere containing an appreciable amount of oxygen and moisture will react with the O_2 and H_2O to form HTO, and HT. Several studies[38-41] have addressed not only the rates of these reactions, but the effects of catalyzing media as well. More recently, Galloway[29,35] analyzed much of the data from these earlier studies and derived an empirical formalism which relates the amount of tritiated water formed to the size of the initial tritium release and time. This formalism also takes account of the anticipated radiation environment in typical fusion

reactor buildings and, therefore, is well suited to the analytical model described herein. The empirical relationship derived by Galloway is given by

$$N_{TO} = \bar{N} \left[1-\exp(-R\bar{N}t)\right] \tag{7}$$

where N_{TO} is the concentration of tritiated water (HTO or T_2O), $\bar{N}$ is the total tritium concentration, and R is the reaction rate constant. Values of R computed by Galloway for humid and dry air are given in Table IV in units that are consistent with the model described in this paper.

Table IV. Summary of Reaction Rate Data for the Oxidation of Molecular Tritium to Water in Moist and Dry Air.

Condition	Reaction Rate, R or 2C ($m^3/\mu Ci \cdot min$)		Reference
	Dry Air	Moist Air	
Static Glass Bulb - No Catalyst	1.0×10^{-14}	———	Casaletto, et al
Static Glass Bulb - No Catalyst	9.3×10^{-15}	4.8×10^{-14}	Eakins and Hutchinson
Static Glass Bulb - Brass	1.0×10^{-14}	1.4×10^{-12}	" "
Static Glass Bulb - Aluminum	6.5×10^{-14}	1.6×10^{-13}	" "
Static Glass Bulb - Steel	7.0×10^{-14}	1.0×10^{-12}	" "
Static Glass Bulb - Platinum	4.0×10^{-13}	1.4×10^{-11}	" "
Inert Atmosphere (Helium)	-	2.5×10^{-14}	Yang and Gevantman
Derived from Literature Data[a]	1.0×10^{-14}	4.8×10^{-14}	Galloway

[a] Galloway[42] has noted a factor of 10^3 discrepancy in his published values[35] due to an error in changing units.

In order to develop a rate expression for the formation of tritiated water, it is necessary to differentiate equation (7) with respect to time, keeping in mind that $\bar{N}$ is also time dependent. This differentiation gives

$$\left(\frac{\partial N_{TO}}{\partial t}\right)_G = G \tag{8}$$

where

$$G = [1-\exp(-R\bar{N}t) + R\bar{N}t\exp(-R\bar{N}t)]\frac{\partial\bar{N}}{\partial t} + R\bar{N}^2\exp(-R\bar{N}t) \quad (9)$$

As an alternative to equation (8) the model also has built into it a more simplified expression based on the data of Eakins and Hutchinson[38] for comparison purposes. Their data were obtained in experimental assemblies with surface area to volume ratios considerably greater than the anticipated ratio for fusion reactor buildings, i.e., $\sim 0.1\ m^2/m^3$. [The data of Eakins and Hutchinson are included among the sets of data used by Galloway to derive equation (7).] Results obtained in the absence of and presence of catalyzing surfaces (e.g., stainless steel, aluminum, brass, and others) were fit to an equation wherein the rate of reaction of T_2 with O_2 and H_2O was taken to be proportional to both the total residual tritium concentration (including all species) and the residual T_2 concentration. Presumably this expression accounts for a reaction that is first order in T_2 concentration but is accelerated by the decay radiation environment resulting from all the tritium that is present. The rate of production of HT and HTO in humid air is, therefore, represented by

$$\left(\frac{\partial N_{HT}}{\partial t}\right)_C + \left(\frac{\partial N_{TO}}{\partial t}\right)_C = 2CN_{T2}\bar{N} \quad (10)$$

where 2C is equal to the rate constant taken from the data of Eakins and Hutchinson.[38] In accord with their findings it was assumed that in humid air the $T_2 + H_2O \rightleftharpoons HTO + HT$ reaction predominates and, therefore,

$$\left(\frac{\partial N_{HT}}{\partial t}\right)_C \simeq \left(\frac{\partial N_{TO}}{\partial t}\right)_C \simeq CN_{T2}\bar{N} \quad (11)$$

Accordingly, in dry air

$$\left(\frac{\partial N_{HT}}{\partial t}\right)_C = 0 \quad (12)$$

and

$$\left(\frac{\partial N_{TO}}{\partial t}\right)_C = 2CN_{T2}\bar{N} \quad (13)$$

Rate constants from the work of Eakins and Hutchinson that were used in the present study are summarized in Table IV.

Permeation of T_2 and HT into Building Surfaces: The permeation of molecular tritium species (T_2 and HT) into building surfaces is dealt with in an approximate manner by summing the permeabilities of all structural surfaces based on an assumed steady-state condition. The aggregate permeability of the enclosure, B, is given by

$$B = \frac{1}{V} \sum_{I=1} \frac{\text{AREA (I)}}{\text{THK (I)}} \phi(I) \exp[Q_p(I)/RT(I)] \qquad (14)$$

where AREA(I) and THK(I) are the area and effective thickness of surface (I), and $\phi(I)$, $Q_p(I)$ and T(I) are, respectively, the permeation coefficient, apparent activation energy, and temperature of material (I). Values of $\phi(I)$ and $Q_p(I)$ were taken directly from the literature where for most cases material (I) was assumed to be stainless steel.

The effective thickness was usually taken to be $\sim$ 1 cm based on a line of reasoning which suggested that permeation rates obtained with this value would be close to the achievable rate for a stainless steel building surface with an $\sim$ 100-X permeation barrier. A more correct way to deal with the permeation term would be to set up a time dependent non-steady-state diffusion calculation since steady-state permeation would never be reached in an actual situation. Because the concentration gradient driving the permeation is near to infinity immediately after the tritium release (i.e., at t = 0) and only approaches the steady-state value with time, the steady-state approach using equation (14) tends to underestimate the initial permeation rate, (i.e., during the early portions of the cleanup operation) by an indeterminant amount. However, for relatively thin surfaces the actual permeation rate should approach the steady-state value rather quickly. By using an effective thickness of 1 cm and the unperturbed permeation parameters for stainless steel, the resulting permeation scenario corresponds to that for stainless steel with a 100-X barrier and an actual thickness of 0.01 cm. Although 0.01 cm is extremely thin for a real situation, it is believed to represent a reasonable estimate of the average effective thickness over the duration of the cleanup operation. Because this rather crude method of

handling the permeation term adds considerable doubt to the permeation related output, all conclusions drawn from permeation effects studies done with TSOAK have to be made discriminately.

Following from the above discussion, the rates of change in concentration of T_2 and HT in the enclosure (N_{T2} and N_{HT}) due to permeation are approximated by

$$-\left(\frac{\partial N_{T2}}{\partial t}\right)_B = B\left[N_{T2}^{1/2} - S_{T2}^{1/2}\right] \tag{15}$$

$$-\left(\frac{\partial N_{HT}}{\partial t}\right)_B = \frac{B}{2}\left[N_{HT}^{1/2} - S_{HT}^{1/2}\right] \tag{16}$$

where a half-power dependence on ambient concentration (i.e., pressure) is employed and where the terms S_{T2} and S_{HT} are adjustable constants that permit the inclusion of an effective concentration of tritium in the enclosure surfaces.* Values of S_{T2} and S_{HT} are usually selected such that during the early portions of the cleanup analysis $N_{T2} >> S_{T2}$ and $N_{HT} >> S_{HT}$ but near the end of the cleanup operation $S_{T2} > N_{T2}$ and $S_{HT} > N_{HT}$. The net result of these added terms is to provide some return of permeated tritium towards the latter stages of enclosure detritiation without grossly affecting the early permeation rate. Again, the actual values of S_{T2} and S_{HT} should be determined as a function of time using a non-steady state summing technique. [A cursory assessment of the type of algorithm required to treat the entire permeation term represented by equations (15) and (16), using non-steady formalisms, indicated that it could be developed but with significant extension in required computer time and with little guarantee that the end result would be any less speculative.]

---

* In dealing with the actual calculations reported further on, it proved advantageous to arbitrarily set $S_{HT} = 0$, since the value of N_{HT} is always much less than N_{T2} for pure T_2 releases and because $S_{HT} \neq 0$ at $t = 0$ causes a perturbation in the initial values of N_{HT}.

Adsorption and Release of HTO and T_2O: The adsorption and release of tritiated water (referred to hereafter as TO) also had to be treated in a highly approximate manner. The rate of adsorption of TO was taken to be proportional to the concentration of TO, N_{TO}, in the enclosure, and the corresponding proportionality constant, E, was determined by summing the estimated adsorptivities of the different surfaces in the enclosure as shown in equation (18)

$$-\left(\frac{\partial N_{TO}}{\partial t}\right)_E = \frac{E}{V} N_{TO} \tag{17}$$

$$E = \sum_{J=1} \alpha\, \gamma(J)\, AABS(J) \tag{18}$$

where α, $\gamma(J)$, and AABS(J) are, respectively, the surface striking rate, the sticking probability of surface (J) (assumed to be material dependent), and the area of surface (J). The rate, ν, at which molecules strike a surface (according to simple kinetic theory) is given[43] by

$$\nu = 3.513 \times 10^{22} \frac{P}{(MT)^{1/2}} \tag{19}$$

where P is the gas pressure in torr, M is the molecular mass in grams, T is the Kelvin temperature, and the unit for ν is molecules/cm^2-s. For HTO (M = 20) at room temperature (T = 300 K) the value of α derived from ν is 7.74×10^3 $\mu Ci/m^2 \cdot min/(\mu Ci$ of $HTO/m^3)$. Evaluation of the sticking probability, $\gamma(J)$, for a given molecule on a given surface requires actual measurements under representative conditions. The basis used in this study for the development of an $\alpha \cdot \gamma(J)$ product value is given below.

By and large the type of data needed for a thorough evaluation of large enclosures with a heterogeneity of surfaces is simply not available. To get some idea of the order of magnitude of the sticking probability for HTO, use was made of the data of Kornacheva et al.[44] for the adsorption of water vapor on oxidized and reduced iron at room temperature. Because their data show that between 10 and 70% relative humidity the amount of adsorbed water varies by less than a factor of two for various states of surface oxidation, the effect of surface condition was ignored and the iron

data were assumed to be representative of steel enclosure surfaces. A mean value for the quantity of adsorbed H_2O at 50% relative humidity is $\sim 10^{19}$ molecules/m^2. This value would correspond to 5×10^5 μCi/m^2 of HTO if the enclosure contained HTO at 50% relative humidity and if the sticking probabilities of HTO and H_2O were essentially the same (a seemingly reasonable assumption). However, the concentration of H_2O molecules at 50% relative humidity in room temperature air is $\sim 4 \times 10^{23}$ molecules/m^3, corresponding to 2×10^{10} μCi of HTO/m^3, while the concentration of tritium in a 10^5 m^3 enclosure after a 100 g T_2 release corresponds to only 10^7 μCi of HTO/m^3. It is clear from the above figures that even in an enclosure with a surface area to volume ratio near 1 m^2/m^3, the total amount of moisture in the enclosure atmosphere is many orders of magnitude greater ($\sim 10^4$ to 10^5) than the amount adsorbed on the walls, and the maximum amount of tritiated water that could be present in the enclosure following a massive tritium release is many orders of magnitude less than the total amount of H_2O already in the enclosure. One can conclude from this that the sticking rate $[\alpha\gamma(J)]$ for HTO molecules at steady-state should be very small and that the amount of tritiated water adsorbed on the enclosure surfaces at long time should be only a few ppm of the total adsorbed moisture. However, in the early stages of a cleanup operation following a sizeable tritium release, the actual sticking rate could be appreciably greater than the steady-state (or long time) value, assuming that the building surfaces are initially free of adsorbed tritium. [Values in the range 10^{-4} to 10^{-7} were used for the $\alpha \cdot \gamma(J)$ product in most analysis, based largely on the results presented in Section 3.5.]

The rate at which adsorbed HTO, S_{TO}, is released from the surface is programmed into the code as follows

$$\left(\frac{\partial S_{TO}}{\partial t}\right)_{E,F} = EN_{TO} - FS_{TO} \tag{20}$$

where F is an adjustable parameter that accounts for the fractional rate of release of adsorbed HTO from the building surfaces. The release term developed in this manner is of course quite arbitrary, but it does permit a real time estimation of the mean rate at which HTO desorption is occurring. In order to solve equation (20), S_{TO} is set equal to zero at t = 0 and the value of S_{TO} used in the right side of equation (20) is developed from the preceding time step in the integration.

Soak Effect and Amount Soaked: The "soak effect", Δ, and the amount of tritium soaked, N_S, are determined, respectively, by:

$$\Delta = (\bar{N}_O - \bar{N})V \tag{21}$$

$$\bar{N}_O = T_O \exp(-At) \tag{22}$$

$$\left(\frac{\partial N_S}{\partial t}\right) = VB(N_{T2}^{1/2} + 0.5\, N_{HT}^{1/2} - S_{T2}^{1/2} - 0.5\, S_{HT}^{1/2}) + EN_{TO} - FS_{TO} \tag{23}$$

where T_O is the instantaneous tritium level at $t = 0$. The "soak effect" is essentially the difference between the amount of tritium in the enclosure under ideal cleanup conditions [i.e., equation (22)] and the amount present under the influence of soaking mechanisms. The actual value of N_S as a function of time is obtained by solving equation (23) together with the other differential equations.

The Resulting Family of Differential Equations: Following from the above developed partial differential equations, it is now possible to assemble a family of interdependent equations which can be solved by digital computer methods as follows:

$$\bar{N} = N_{T2} + N_{TO} + N_{HT} \tag{24}$$

$$-\frac{dN_{T2}}{dt} = AN_{T2} + B(N_{T2}^{1/2} - S_{T2}^{1/2}) + 2CN_{T2}\,\bar{N} + G \tag{25}$$

$$-\frac{dN_{TO}}{dt} = AN_{TO} + \frac{E}{V} N_{TO} - CN_{T2}\,\bar{N} - G - \frac{F}{V} S_{TO} \tag{26}$$

$$-\frac{dN_{HT}}{dt} = AN_{HT} + \frac{B}{2} N_{HT}^{1/2} - CN_{T2}\,\bar{N} \tag{27}$$

$$-\frac{dN_S}{dt} = VB(N_{T2}^{1/2} + 0.5\, N_{HT}^{1/2} - S_{T2}^{1/2} - 0.5\, S_{HT}^{1/2}) + EN_{TO} - FS_{TO} \tag{28}$$

$$\frac{dS_{TO}}{dt} = EN_{TO} - FS_{TO} \tag{29}$$

$$G = [1-\exp(-R\bar{N}t) + R\bar{N}t\exp(-R\bar{N})]\,\frac{d\bar{N}}{dt} + R\bar{N}^2\exp(-R\bar{N}t) \quad (30)$$

$$\Delta = (\bar{N}_0 - N)\,V \quad (31)$$

Equations (24) through (31) were programmed into a driver subroutine that was then coupled to an existing differential equation solver package. Details of the computer code are given in Appendix A of reference 45.

3.3 Application of the Soaking Code to a Typical Reactor Building

In order to evaluate the application of TSOAK to a typical reactor building, a set or representative parameters were developed based on current projections for near-term tokamak reactors.[30,46] Results of soaking calculations for a "base case" scenario involving the cleanup of tritium releases in the range 2 to 200 grams to a 1.6×10^5 m^3 room by a 5 m^3/s air detritiation system are presented in Table V. Also shown in Table V are the results obtained by varying selected "base case" parameters. As indicated in the table, the amount soaked and the cleanup time are most sensitive to air flow rate. However, inclusion of 20 m^2 of cold surface, which is simulated by a sticking probability near unity coupled with a somewhat higher long-term release coefficient (+ 20 m^2 @ < 0°C in Table V), led to the prediction of a considerably extended cleanup time due to the slow back release of condensed HTO.

Graphical computer output for the "base case" and the case involving the simulated cold surface are given in Figures 20 and 21. The two solid curves in Figure 20a correspond to the ideal cleanup response (lower plateauing curve), and the TSOAK calculated response for the base case (upper plateauing curve). The plateauing of the cleanup curves (solid lines) in Figures 20a and 21a results from the inclusion of a 4 $\mu Ci/m^3$ asymptote to more realistically represent the kinds of terminating effects (due to background signals) that may be encountered in actual monitoring operations. The need for this asymptote is more clearly evident from the results reported in the next two sections. The abrupt termination in the "soak effect" and "amount soaked" curves in Figure 21a is a result of oscillations that develop in the differential equation solver when the amount of soaked tritium is large compared to the amount of tritium remaining in the enclosure atmosphere.

Table V. Selected Results of Air Cleanup Calculations Using TSOAK

Base Case Parameters:

Building Volume	= 1.6×10^5 m^3	Reaction Rate	= 1.5×10^{-11} m^3/μCi·min
Process Efficiency	= 1.0 (100%)	HTO Adsorption Rate	= 1.0×10^{-7}/m^2·min
Air Flow Rate	= 5 m^3/s	HTO Release Rate	= 1.0×10^{-4}/min
Building Surface Area	= 2×10^4 m^2	S_{T2}[a]	= 0 μCi/m^3

Conditions	Release Size (g)	Amount Soaked (Ci)	Cleanup Time (hr)
Base Case	200	6.3×10^{-1}	142
	20	6.8×10^{-3}	125
	2	7.0×10^{-5}	100
Base Case + Increase Air Flow Rate by 10-X	200	7.6×10^{-3}	14
	20	7.7×10^{-5}	12
	2	7.7×10^{-7}	10
Base Case + Increase Reaction Rate by 100-X	200	6.0×10^{0}	142
	20	3.6×10^{-1}	125
	2	6.5×10^{-3}	100
Base Case + Increase Adsorption Rate by 100-X	200	$\leq 5.0 \times 10^{1}$	Tailing
	20	6.8×10^{-1}	125
	2	6.7×10^{-3}	100
Base Case + 200 m^2 of SS at 300°C (Permeation Test)	200	2.1×10^{1}	142
	20	6.4×10^{0}	125
	2	2.0×10^{0}	100
Base Case + 200 m^2 of SS at 300°C and BPT = 50 μCi/m^3 (Back Permeation Test)	200	2.1×10^{1}	142
	20	6.0×10^{0}	125
	2	1.6×10^{0}	100
Base Case + 20 m^2 at 50°C	20	6.3×10^{1}	Tailing

[a] S_{T2} = the average equivalent concentration of tritium in the high-temperature stainless steel (SS) that is contributing to back-permeation of tritium into the building.

3.4 Bench Scale Tests of Air Detritiation

In order to provide a test of the computer model for air detritiation analysis, a bench scale experiment was set up to simulate, at least in part, the conditions anticipated for larger enclosures following a tritium release. The experimental assembly, diagrammed in Figure 22, consisted of an ∿ 50-liter cubical plastic desiccating box with a flat plexiglass door clamped to one face of the box and sealed by a circumferential rubber gasket. This box (hereafter referred to as the enclosure) was attached to two separate gas circulation loops. One loop (monitoring loop) was connected directly to a flow-through type tritium monitor (Triton Model 955B) having its own internal circulation pump. The other loop (processing loop) consisted of a flow meter, an oxidizer bed (Hopcalite) operated at ∿ 550°C, a moisture trapping bed

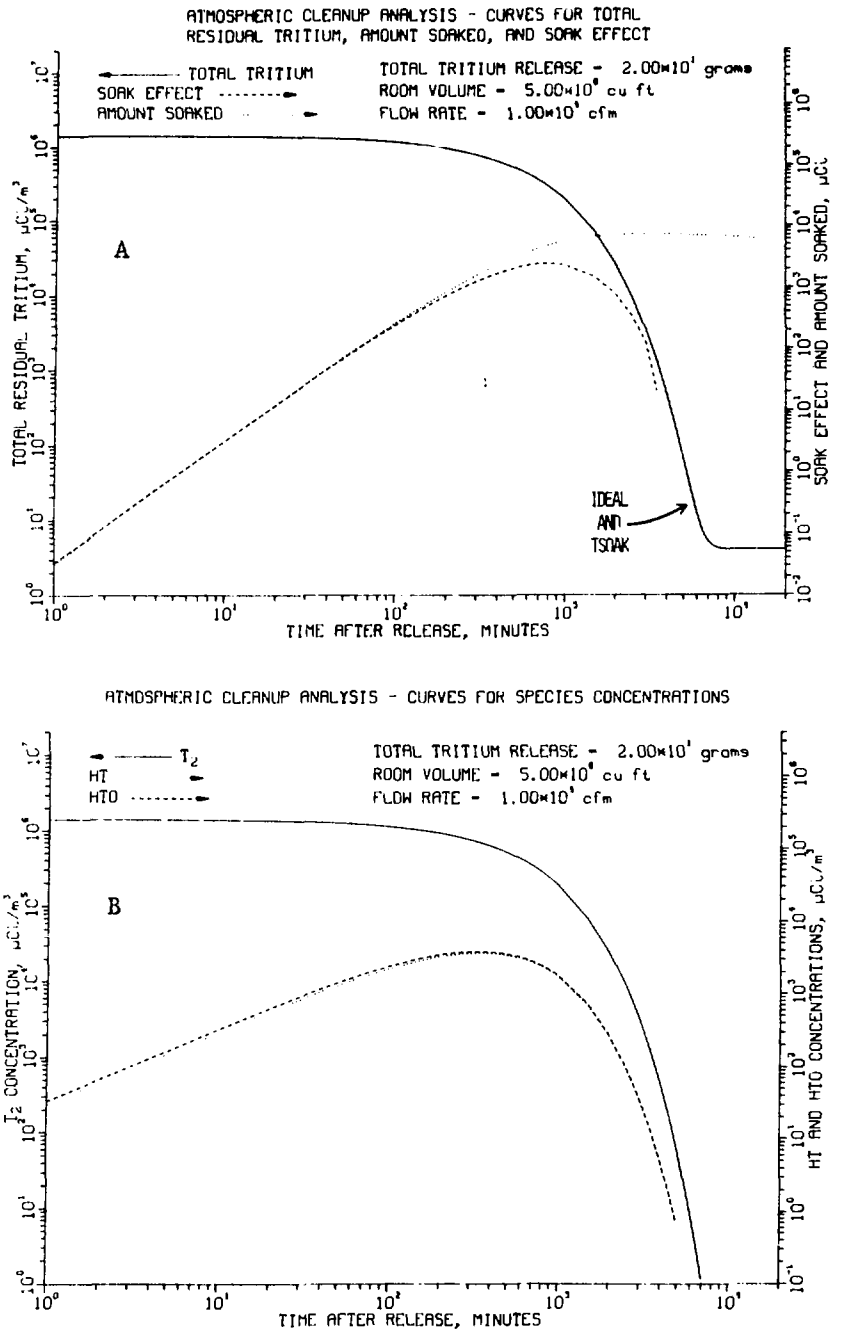

Figure 20. Graphical Representation of TSOAK Calculations for a "Base Case" Scenario of a 20-g T_2 Release (see Table V and text). The total tritium concentration, soak effect and amount soaked as functions of time are given in Figure 20a. The concentrations of T_2, HTO, and HT as functions of time are given in Figure 20b.

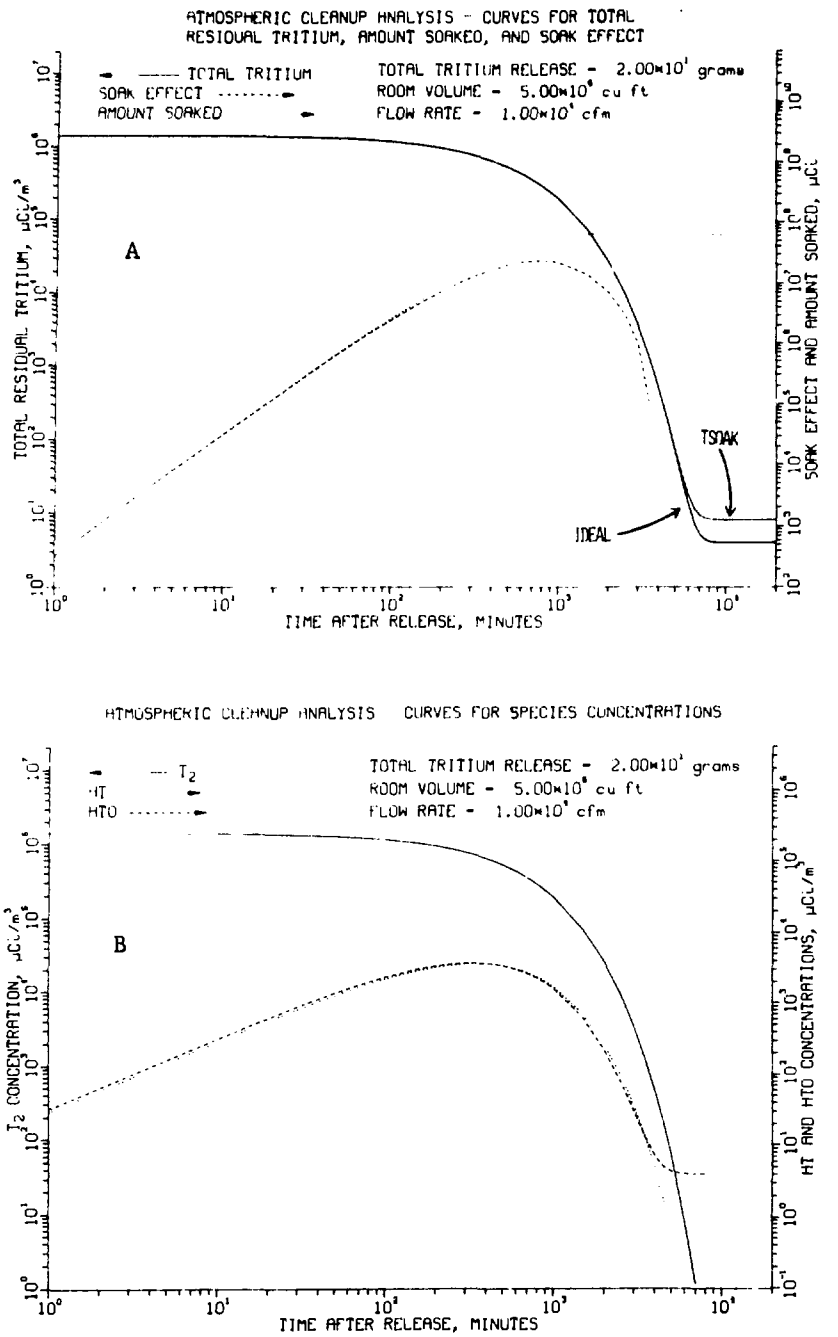

Figure 21. Graphical Representation of TSOAK Calculations for the "Base Case" Scenario of a 20-g T_2 Release, Modified to Include 20 m^2 of Condensing Surface (i.e., at ≤ 0°C). The total tritium concentration, soak effect, and amount soaked as functions of time are given in Figure 21a. The concentrations of T_2, HTO and HT as functions of time are given in Figure 21b.

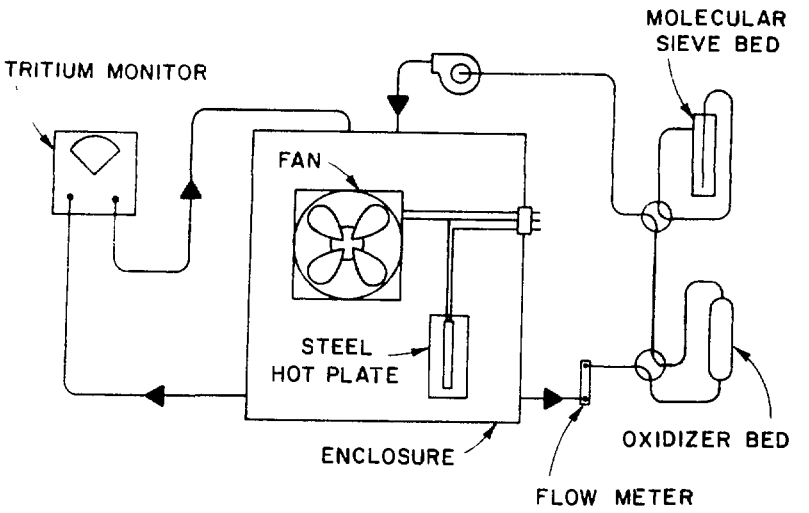

Figure 22. Apparatus for Bench-Scale Air Detritiation Studies.

(#4A molecular sieve) operated on 0°C, and a diaphragm-type circulation pump. Typical experiments were carried out by (1) injecting enough tritium as T_2 to raise the tritium level in the enclosure to from 1000 to 3000 $\mu Ci/m^3$, (2) circulating the enclosure atmosphere through the monitoring loop until a stable tritium signal was achieved, and then (3) starting up circulation through the processing loop.

To a first order of approximation, a cleanup operation carried out in the manner described above should proceed with a simple exponential dependence on time as given by equation (22). In actual practice, the uncertainties in measuring flow rate and enclosure volume (at best a few percent in each case), coupled with the fact that the efficiency is near unity, make it diffucult to determine the extent to which equation (22) is obeyed. This is important because, when the trapping efficiency is only slightly less than unity, a significant amount of tritiated moisture can be transported back to the enclosure. The consequences of these uncertainties should be borne in mind when considering the results described below.

Figure 23 shows the results of typical detritiation simulations on the enclosure. The apparent obeyance of equation (22) persists from the starting point (t = 0, $N_T \simeq 1300$ $\mu Ci/m^3$) to an N_T value roughly 40 times lower, after which a pronounced tailing of each cleanup curve is observed. In order to perform the experiments shown in Figure 23, an electrical feed-through was adapted to the enclosure to permit operation (inside the enclosure) of a circulation fan and a calrod heated stainless steel plate with $\sim$ 200 cm^2 of surface area. As indicated in Figure 23, the curves therein represent results of cleanup operations performed on the enclosure for various sets of operating conditions involving the fan and heated plate. Operation of the fan during detritiation (Case B) seems to enhance the tailing effect, possibly by accelerating the rate of the reaction/adsorption/release mechanisms involving HT and, more importantly, HTO. Operation of the hot plate at $\sim$ 200°C together with the fan (Case C) demonstrated only moderately different detritiation characteristics relative to Case B. Although the hot plate might be expected to cause an increase in the rate of HTO formation, it also raises the enclosure atmosphere temperature by $\sim$ 20°C, which would tend to reduce the amount of adsorbed HTO.

During other experiments, like the ones in Figure 23, one or the other, and in some cases both, of the processing steps (oxidation and water stripping) were temporarily by-passed. When both processing steps are by-passed at a point in time after the tailing has begun, the tritium level in the enclosure usually tends to rise slowly with time, sometimes increasing overall by as much as 50 to 100%. Further, most of the residual tritium that is present after tailing has been reached can be removed from the enclosure simply by reinserting the molecular sieve bed alone. This result implies that, near the end of the simulated cleanup operation, a large fraction of the tritium present in the enclosure is in the oxidized form (HTO) -- perhaps the result of incomplete trapping of water by the molecular sieve bed.

3.5 Computer Fitting of the Bench Scale Data

Following the experimental studies described in the preceding section, an attempt was made to derive reaction rate constants, HTO adsorption coefficients, and HTO desorption coefficients for the enclosure cleanup curves using TSOAK. By properly adjusting these three parameters it was possible

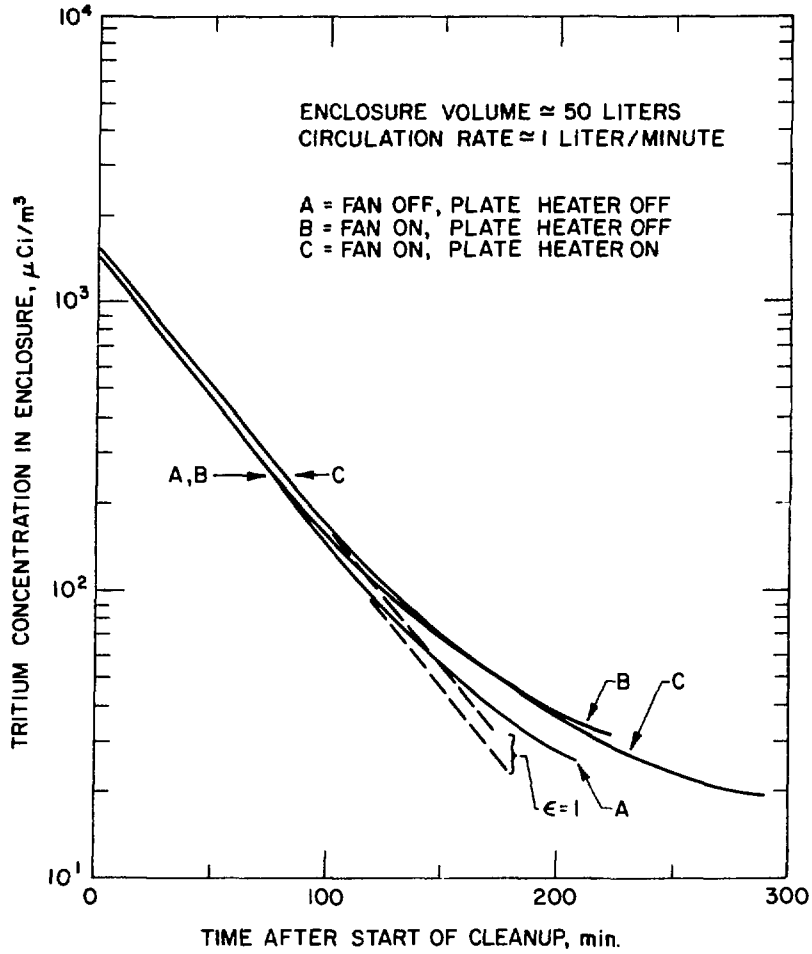

Figure 23. Cleanup Curves for Various Operating Modes with the Small-Scale Air Detritiation Apparatus.

to obtain exact fits to the experimental curves. The observed cleanup curves for two experimental cases are compared to the corresponding ideal cleanup curves in Figure 24. Also shown in the figure are the data points for the TSOAK fit to the observed curve. (An asymptote of 4 $\mu Ci/m^3$ was used in both the ideal and TSOAK calculations, and it is this asymptote which causes the curvature in the ideal curve.)

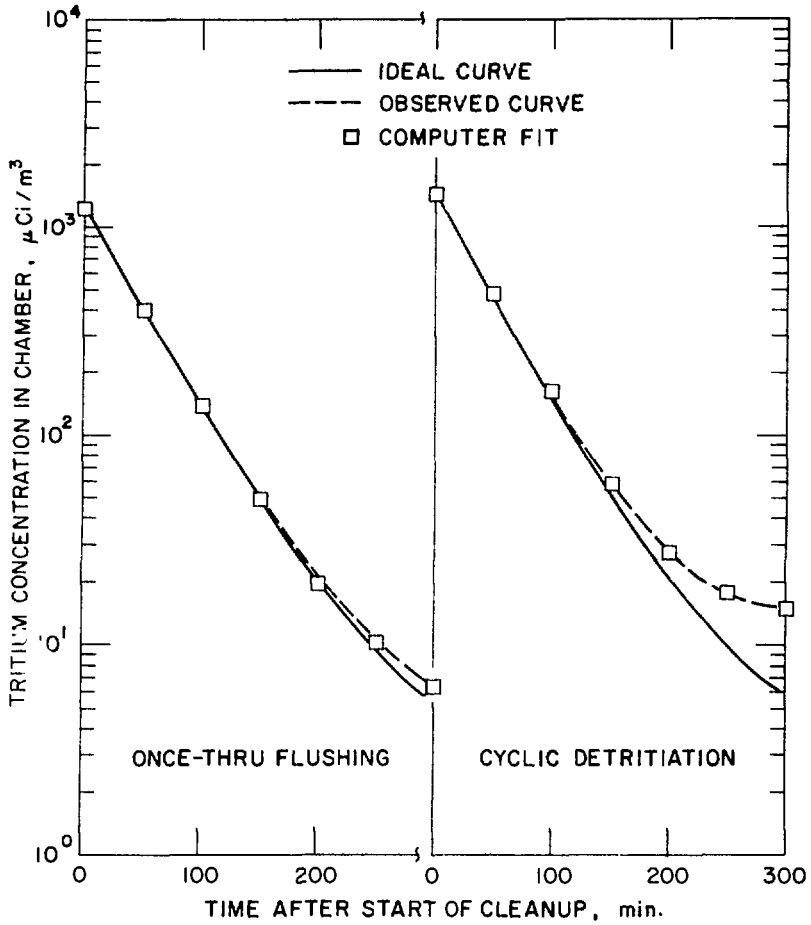

Figure 24. Comparison of Observed Versus Ideal and TSOAK Calculated Results for Two Air Detritiation Experiments. (Flow rate - 1 liter/min., enclosure volume ≃ 50 liters.)

The experiment plotted on the left hand side of Figure 24 was performed by pulling clean air into the enclosure and exhausting the exit gas to a fume hood. This experiment, therefore, represents the condition of having a 100% efficient scrubbing system. The experiment plotted on the right hand side of Figure 24 was performed under identical conditions (release size, flow rate, etc.) except that the enclosure atmosphere was circulated in a closed loop through the oxidizer bed and molecular sieve bed. The increased departure from ideal behavior in the latter case (compared to the once-through flushing case) is most probably attributable to a less than 100% HTO scrubbing efficiency of the molecular sieve bed. While on first thought

this appears to be the result of having an inadequately designed scrubbing system, it does not take much of a departure from 100% efficiency to create a sizeably increased apparent HTO production rate in the enclosure, i.e., less than 1% reduction in efficiency would be more than adequate to explain the differences in Figure 24. Table VI lists the TSOAK derived fitting parameters for the two experiments in Figure 24 and for two other interesting cases as well. Particularly worthy of note are the substantial increases in all three parameters when the fan and hot plate are both operating. The 400-fold increase in the required reaction rate parameter is considered to be well above the uncertainties associated with the computer model and with the experiment itself.

Table VI. Summary of Curve Matching Parameters Obtained from TSOAK Fits to Enclosure Detritiation Experiments.

Condition	Reaction Rate Parameter,[a] ($m^3/\mu Ci$-min)	Absorption Rate Parameter,[b] ($\mu Ci/m^2$-min)	Release Rate Parameter,[c] (%/min)
Typical Literature Data	10^{-12}-10^{-14}	--	--
Enclosure Fan Off, Plate Cool	1×10^{-5}	3×10^{-4}	3
Enclosure Fan On, Plate Cool	5×10^{-5}	2×10^{-4}	3
Enclosure Fan On, Plate Hot[d]	4×10^{-4}	5×10^{-5}	12
Enclosure Once-Through Flushing	1×10^{-6}	2×10^{-4}	3

[a] Reaction Rate = Reaction Rate Parameter x $\bar{N}$ x N_{T2}

[b] Absorption Rate = Absorption Rate Parameter x N_{TO}

[c] Release Rate = Release Rate Parameter x S_{TO}

[d] Plate heated to $\sim$ 200°C.

3.6 Conclusions

Although the results of the soaking studies described above are considered to be largely of semi-quantitative significance only, several conclusions can be drawn from the work carried out to date. These may be stated summarily as follows: (1) When the relative humidity is greater than a few percent, the total amount of adsorbed tritiated water is greatly reduced due to surface swamping by H_2O. (2) Exposed elevated temperature metal surfaces ($\geq$ 200°C) represent a major reaction and soaking pathway. All thermally hot metal surfaces should be insulated and preferably isolated from the building atmosphere. (3) Exposed low temperature surfaces ($\geq$ 0°C) are also undesirable. Such surfaces (simulated by using sticking probabilities near unity) need not be large in area to condense large quantities of tritiated water. (4) For rooms in the range 10^4 to 10^5 m^3 (10^6 to 10^7 cu.ft.), a 50 m^3/s (10^5 cfm) processor is desirable and 0.5 m^3/s (10^3 cfm) is inadequate. With judicious selection of building materials, surface preparation procedures, and atmosphere operating parameters, a 5 m^3/s (10^4 cfm) system (near to state-of-the-art system) could be acceptable.

The principal value of predominantly empirical studies of the type described in this report is that they represent a medium with which results of actual detritiation experiments can be compared and correlated. Perhaps even more importantly they can (if properly used) provide a basis for the conception, design, and operation of meaningful large scale air detritiation tests.

4.0 CONCLUSION

The CINDA-3G computer code was adopted to analyze the operating conditions and thermal responses of two fusion reactor first-wall concepts under normal cyclic plasma burns. The present study and results were based on the actual burn-cycle dynamics calculated for the ANL-EPR, although the code has sufficient flexibility to cover a range of reactor parameters. The two basic first-wall configurations were a bare, water-cooled steel wall and a 1-cm thick graphite liner that radiated its absorbed energy to a water-cooled steel vacuum vessel. The peak steel temperature in the first case was 402°C and the corresponding water temperature was 317°C for an average wall loading of 1.0 MW/m^2, burn time of 65 s, and a dwell time of 30 s. The same conditions for the composite wall case gave the peak graphite surface temperature of 1545°C and the maximum ΔT through the 1-cm liner was 256°C. The surface temperature of the graphite liner is very sensitive to the values of the thermal conductivity for graphite. The surface temperature of the graphite becomes unacceptably high if the lower values of conductivity are used or if the neutron wall loading is increased to 2 MW/m^2 with an average value of 10 $W/m \cdot °K$ for the conductivity of graphite.

The safety studies on thermal responses of tokamak reactor first wall to a plasma dump analyzed the ablative behavior of stainless steel and graphite first walls. The thicknesses of ablated regions were determined parametrically for the two wall materials in terms of the plasma dump time and the fraction of the wall area over which the energy was deposited. If the plasma thermal energy and stored magnetic energy are deposited over more than 50% of the wall, the maximum ablated region is < 70 μm for stainless steel and < 30 μm for graphite. Since it is expected that the plasma energy will be deposited over a major fraction ($> 50\%$) of the first wall during a disruption, it was concluded that both wall materials should withstand a moderate number of disruptive events.

The studies on the vacuum wall electrical resistance requirements in lieu of a ceramic-type flux breaker involved analyses from a multidisciplinary standpoint. The most serious problems seem to be in designing an acceptable

initiation-trimming coil and in designing a vacuum wall that can withstand the pressure and heat loads following a plasma dump. There appear to be several design approaches for the vacuum wall that can achieve a fairly high resistance and may satisfy the latter constraints. Work is continuing to further resolve the limit of the constraints.

The safety studies on air detritiation encompassed modeling and experimental studies that are empirical but represent a medium with which results of actual detritiation experiments can be compared and correlated. The bench-scale soaking studies, together with the modeling effort, permit several conclusions to be drawn: (1) when the relative humidity is greater than a few percent, the total amount of adsorbed tritiated water is greatly reduced due to surface swamping by H_2O, (2) exposed elevated temperature metal surfaces ($\geq 200°C$) represent a major reaction and soaking pathway, all thermally hot metal surfaces should be insulated and preferably isolated from the building atmosphere, (3) exposed low-temperature surfaces ($\leq 0°C$) are undesirable and such surfaces (with sticking probabilities near unity) need not be large in area to condense large quantities of tritiated water, and (4) for space in the range 10^4 to 10^5 m^3 (10^6 to 10^7 cu. ft.), a 50 m^3/s (10^5 cfm) processor is desirable and 0.5 m^3/s (19^3 cfm) is inadequate; with judicious selection of building materials, surface preparation procedures and atmosphere operating parameters, a 5 m^3/s (10^4 cfm) system near to the state-of-the-art system could be acceptable.

References

1. Chrysler Corporation, "Chrysler Improved Numerical Differencing Analyzer for Third Generation Computers," Engineering Department Technical Note, TN-AP-67-287 (October, 1967).

2. S. J. Hakim and R. J. Henninger, Argonne National Laboratory, private communication.

3. W. M. Stacey, Jr., et al., "EPR-77: A Revised Design for the Tokamak Experimental Power Reactor," Argonne National Laboratory, ANL/FPP-77-1 (1977).

4. W. M. Stacey, Jr., et al., "Tokamak Experimental Power Reactor Conceptual Design," Argonne National Laboratory, ANL/CTR-76-3 (1976).

5. "Experimental Power Reactor Conceptual Design Study," General Atomic Company, GA-A14000 (1976).

6. H. C. Stevens, et al., "Tokamak Experimental Power Reactor Primary Energy Conversion System," Second Topical Meeting on Technology of Controlled Nuclear Fusion, Richland, Washington, CONF-760935-P4 (September, 1976).

7. Chrysler Corporation, "Chrysler Improved Numerical Differencing Analyzer for Third Generation Computers," Engineering Department Technical Note, TN-AP-67-287 (October, 1967).

8. W. M. Stacey, Jr., et al., "Plasma Engineering Studies for the Tokamak Experimental Power Reactor," Seventh IEEE Symposium on Engineering Problems of Fusion Research, Knoxville, Tennessee (October, 1977).

9. M. A. Abdou, "Nuclear Design of the Blanket/Shield System for a Tokamak Experimental Power Reactor," *Nuclear Technology*, 29, 7 (1976).

10. S. J. Hakim and R. J. Henninger, "USEFUL: A Hydrodynamic Code for Treating Flow and Freezing in Annular, Pipe and Plate Geometries," Argonne National Laboratory, ANL/RAS-77-25 (1977).

11. C. S. Kim, "Thermophysical Properties of Stainless Steel," Argonne National Laboratory, ANL-75-55 (1975).

12. R. T. Dolloff and J. T. Meers, "Status and Future of Graphite and Refractory Compounds," in High Temperature Materials, II, Interscience Publishers, New York, 387 (1963).

13. M. R. Everette, et al., "Dimensional and Physical Property Changes of High-Temperature Reactor Graphites," *Carbon*, 9, 417 (1971).

14. G. B. Engle, "Irradiation Behavior of Nuclear Graphites at Elevated Temperatures," *Carbon*, 9, 539 (1971).

15. M. A. Abdou and C. W. Maynard, "Calculational Methods for Nuclear Heating -- Parts I and II," *Nuclear Science and Engineering*, 56, 360 (1975).

16. W. M. Stacey, Jr., et al., "Tokamak Experimental Power Reactor," Argonne National Laboratory, ANL/FPP/TM-93; also to be published in *Nuclear Fusion*.

17. T. H. Stix, *Physics Review Letters*, 30, 833 (1973).

18. J. C. Hosea, et al., "Stability Experiments on the ST Tokamak," Plasma Physics and Controlled Nuclear Fusion Research, IAEA, Vienna (1971), Vol. 2, p. 425.

19. V. S. Vlasenkov, et al., "Perturbation of a Magnetic Field During the Break-up Instability in Tokamak-6," Plasma Physics and Controlled Nuclear Fusion Research, IAEA, Vienna (1971), Vol. 1, p. 33.

20. K. Karger, et al., "On the Origin of the Disruptive Instability in the Pulsator Tokamak," Plasma Physics and Controlled Nuclear Fusion Research, IAEA, Vienna (1971), Vol. 1, p. 267.

21. S. V. Mirnov, et al., "Observation of Disruptive-Instability Fine Structure in a Tokamak," Plasma Physics and Controlled Nuclear Fusion Research, IAEA, Vienna (1971), Vol. 1, p. 291.

22. H. Toyama, et al., "Experiments on Noncircular Tokamak and Related Topics," Plasma Physics and Controlled Nuclear Fusion Research, IAEA, Vienna (1971), Vol. 1, p. 323.

23. G. Cima, et al., "Shaping and Compression Experiments in a Tokamak," Plasma Physics and Controlled Nuclear Fusion Research, IAEA, Vienna (1971), Vol. 1, p. 335.

24. I. H. Hutchinson, *Physics Review Letters*, 37, 338 (1976).

25. R. A. Jacobsen, *Plasma Physics*, 17, 547 (1975).

26. A. H. Morton, *Nuclear Fusion*, 16, 571 (1976).

27. D. B. Albert, et al., *Nuclear Fusion*, 17, 863 (1977).

28. L. J. Wittenberg, "Evaluation Study of the Tritium-Handling Requirements of a Tokamak Experimental Power Reactor," Mound Laboratory Report, MLM-2259 (November, 1975).

29. T. R. Galloway, et al., "Mirror Reactor Blankets," Proceedings of the Magnetic Fusion Energy Blanket and Shield Workshop, USERDA Report 76/117/2, pp. 504-535 (August, 1975).

30. W. M. Stacey, Jr., et al., "Tokamak Experimental Power Reactor Conceptual Design," Argonne National Laboratory, ANL/CTR-76-3, pp. X-1 - X-33 (August, 1976).

31. J. L. Anderson, F. A. Damiano and J. E. Nasise, "Tritium Handling Facilities at the Los Alamos Scientific Laboratory," Proceedings of the 23rd Conference on Remote Systems Technology, 1975 ANS Winter Meeting, San Francisco, California, November 16-25, 1975.

32. P. D. Gildea, "Containment and Decontamination Systems Planned for the Tritium Research Laboratory Building at Sandia Laboratories, Livermore," Proceedings of the International Conference on Radiation Effects and Tritium Technology for Fusion Reactors, CONF-750989 (1976) p. 111-112.

33. T. B. Rhinehammer and P. H. Lamberger, "Tritium Control Technology," USAEC Report WASH-1269 (1973).

34. C. J. Kershner, "Tritium Effluent Control Project at Mound Laboratory," Proceedings of the Symposium on Tritium Technology Related to Fusion Reactor Systems, USERDA Report ERDA-50 (1975) p. 50.

35. T. R. Galloway, "A Containment and Recovery System for Fuel Reprocessing Plants," Proceedings fo the 14th ERDA Air Cleaning Conference, Sun Valley, Idaho, August 11, 1976.

36. W. M. Rodgers and R. Michalek, "Tritium Removal Systems, "Report published by Engelhard Industries Division of Engelhard Minerals and Chemicals Corporation.

37. J. C. Bixel and C. J. Kershner, "A Study of Catalytic Oxidation and Oxide Adsorption for the Removal of Tritium from Air," Proceedings of the Second AEC Environmental Protection Conference, USAEC Report WASH-1332 (1974) p. 261.

38. J. D. Eakins and W. P. Hutchinson, "The Radiologic Hazard from the Conversion of Tritium to Tritiated Water in Air by Metal Catalysts," in Tritium, A. A. Moghissi and M. W. Carter, Eds., Messenger Graphics, Phoenix, Arizona (1973).

39. L. F. Belovodskii, et al., "Oxidation of Tritium in Air under the Action of Intrinsic Radiation," *Atomnaya Energiya*, 38 (1975) p. 379.

40. J. Y. Yang and L. H. Gevantman, "Tritium β-Radiation-Induced Isotopic Exchange with Water Vapor," *J. Phys. Chem.*, 68 (1964) p. 3115.

41. G. J. Cassaletto, L. H. Gevantman and J. B. Nash, "The Self-Radiation Oxidation of Tritium in Oxygen and Air," U. S. Naval Radiological Defense Laboratory Report, US-NRDL-UR-565 (May, 1962).

42. T. R. Galloway, Lawrence Livermore Laboratory (personal communication).

43. S. Dushman, Scientific Foundations of Vacuum Technique, Second Edition, J. M. Lafferty, Ed., John Wiley and Sons, New York (1962) p. 14.

44. G. M. Kornacheva, et al., "The Adsorption of Water Vapor on Iron," *Elektrokhimiya*, 9 (1973) p. 81.

45. R. G. Clemmer, R. H. Land, V. A. Maroni and J. M. Mintz, "Simulation of Large Scale Air Detritiation Operations by Computer Modeling and Bench Scale Experimentation," Argonne National Laboratory, ANL/FPP-77-3 (November, 1977).

46. "TNS Scoping Studies: Interim Status Report for October 1976 - March 1977," Prepared by the TNS Project Staffs of General Atomic Company, GA-A14412, and Argonne National Laboratory, ANL/FPP-77-2 (May, 1977).

Distribution for ANL/FPP/TM-111

Internal:

R. Avery
C. C. Baker
J. N. Brooks
F. A. Cafasso
I. Charak
R. Clemmer
J. B. Darby
S. A. Davis
D. A. Ehst
B. R. T. Frost
L. R. Greenwood
D. M. Gruen
S. D. Harkness
J. C. Jung
M. S. Kaminsky
Y-K. Kim
R. L. Kustom
R. H. Land
V. A. Maroni
R. L. Martin
F. V. Nolfi
J. H. Norem
P. J. Persiani
E. G. Pewitt
D. L. Smith
H. C. Stevens
C. E. Till
L. R. Turner
D. Weber
FP Program (60)
A. B. Krisciunas
ANL Contract File
ANL Libraries (5)
TIS Files (6)

External:

DOE-TIC, for distribution per UC-20e (153)
Manager, Chicago Operations Office
Chief, Chicago Patent Group
President, Argonne Universities Association
Applied Physics Division Review Committee:
  P. W. Dickson, Jr., Westinghouse Electric Corp.
  R. L. Hellens, Combustion Engineering, Inc.
  W. B. Loewenstein, Electric Power Research Inst.
  R. F. Redmond, Ohio State U.
  R. Sher, Stanford U.
  D. B. Wehmeyer, Detroit Edison Co.
  S. A. Werner, U. Missouri
Chemical Engineering Division Review Committee:
  C. B. Alcock, U. Toronto
  R. C. Axtmann, Princeton U.
  R. E. Balzhiser, Electric Power Research Inst.
  J. T. Banchero, U. Notre Dame
  T. Cole, Ford Motor Co.
  P. W. Gilles, U. Kansas
  R. I. Newman, Allied Chemical Corp.
  G. M. Rosenblatt, Pennsylvania State U.
ZGS Complex Review Committee:
  R. L. Cool, Rockefeller U.
  V. W. Hughes, Yale U.
  J. D. Jackson, U. California, Berkeley
  W. Lee, Columbia U.
  H. A. Neal, Indiana U.
  J. L. Rosen, Northwestern U.
  L. C. Teng, Fermi National Accelerator Lab.
M. A. Abdou, Georgia Inst. Technology
J. Baublitz, Office of Fusion Energy, USDOE
S. L. Bogart, Office of Fusion Energy, USDOE
J. M. Mintz, General Atomic
T. Ohkawa, General Atomic
W. M. Stacey, Georgia Inst. Technology
K. M. Zwilsky, Office of Fusion Energy, USDOE